# The Thermal Behaviour of Segregated Heat Sink Structures in Natural Convection


UNIVERSITY of LIMERICK

OLLSCOIL LUIMNIGH

Kevin John O'Flaherty B.Eng.

For the award of a Master's Degree

University of Limerick

Supervisor: Dr. Jeff Punch

Submitted to the University of Limerick, May 2017

# Abstract

Remotely deployed wireless devices such as tower-top active antenna arrays, remote radio heads, and pico or femto-cells are an increasingly prevalent feature of communications systems. Environmental standards which govern outdoor wireless equipment stipulate stringent conditions: high solar loads (up to 1 $kW/m^2$), ambient temperatures as high as 55ºC and negligible wind speeds (0 m/s). These challenges result in restrictions on power dissipation within a given envelope, due to the limited heat transfer rates achievable with natural convection.

There are two main objectives of this thesis; the first is to compare the results from a numerically modelled natural convection heat sink, representative of a remote radio head, with and without a solar shield subject to industrial standards and an environmentally defined worst case condition (a daytime condition in a hot location). The impact of solar shield length and location of the heat sink within the solar shield are investigated. The second main objective of this thesis is to segregate the components within a remote radio head across two heat sinks to improve the heat dissipation of the temperature sensitive components. The primary heat sink, representative of the temperature sensitive components, is experimentally and numerically investigated with and without a shield and without wind or solar loading. A secondary heat sink, representative of high power devices, is added to the shielded configuration in order to create a segregated structure. The secondary heat sink is investigated to determine the impact of the location and the number of fins to maximise the heat transfer on the primary heat sink.

The deployment of a solar shield which is longer than the device that it contains was found to increase heat dissipation through a ‘chimney flow’ effect and it was determined that the heat sink should be located at the base of the solar shield. For a segregated structure, a secondary heat sink with a base plate temperature of 65°C above ambient was found to increase the Nusselt number of the primary heat sink by over 50 % in comparison to an unshielded case. The optimization of the number of fins on the secondary heat sink was found to offer an enhancement of 80 % over an unshielded heat sink.

The findings of this thesis are of practical relevance for the thermal design of outdoor communications equipment: in particular, it is evident that the use of standard environmental conditions is conservative in comparison with a more comprehensive design process which references representative worst case data.

# Acknowledgements

*To my siblings, Cathy, Niamh and Paul; and my parents, Mairead and John, for their guidance and support.*

# Table of Contents

# List of Figures

# List of Tables

# Nomenclature

| Symbol | Description | Units |
|---|---|---|
| a | Face area vector | $m^2$ |
| A | Area | $m^2$ |
| B | Base plate thickness | m |
| $C_p$ | Specific heat capacity | J $kg^{-1}$ $K^{-1}$ |
| El | Elenbaas number | |
| f | Buoyancy induced body forces | N |
| F | View factor | |
| g | Gravitational acceleration, 9.81 m $s^{-2}$ | m $s^{-2}$ |
| Gr | Grashof number | |
| H | Height | m |
| h | Heat transfer coefficient | W $m^{-2}$ $K^{-1}$ |
| I | Identity matrix | |
| k | Thermal conductivity | W $m^{-1}$ $K^{-1}$ |
| L | Length | m |
| m | Fin parameter | |
| N | Number of fins | |
| Nu | Nusselt number | |
| P | Power | W |
| Pr | Prandtl number | |
| Q | Heat dissipation | W |
| $q_s$ | Heat flux from solar irradiation | W $m^{-2}$ |
| q'' | Heat flux vector | W |
| R | Resistance | Ω |
| Ra | Rayleigh number | |
| S | Fin spacing | m |
| $S^*$ | Non-dimensional fin spacing | |
| t | Fin thickness | m |
| T | Temperature | K |
| T | Viscous stress tensor | |
| v | Velocity vector | m $s^{-1}$ |
| V | Voltage | V |
| $V$ | Cell volume | $m^3$ |
| $x$ | | |

| | | |
|---|---|---|
| W | Width | m |
| **Greek letters** | **Description** | **Units** |
| α | Thermal diffusivity | $m^2 s^{-1}$ |
| β | Thermal expansion coefficient | $K^{-1}$ |
| ε | Emissivity | |
| $\eta$ | Fin efficiency | |
| $\mu$ | Dynamic viscosity | $N s m^{-2}$ |
| ν | Kinematic viscosity | $m^2 s^{-1}$ |
| ρ | Density | $kg m^{-3}$ |
| σ | Stefan–Boltzmann constant, $5.669 \times 10^{-8}$ | $W m^{-2} K^{-4}$ |
| χ | Porosity | |

**Subscript**

| | |
|---|---|
| amb | Ambient |
| bot | Bottom surface of the heat sink |
| bp | Base plate heat sink |
| c | Corrected |
| channel | Channel |
| f | Fluid |
| fin | Fin |
| g | Grid |
| h | Heaters |
| h1 | First cartridge heaters |
| h2 | Second cartridge heaters |
| hs | Heat sink |
| IR | Infrared |
| l | Laminar flow |
| opt | Optimum spacing |
| p | Pressure |
| pp | Parallel plates |
| r | Radiation |
| R | Resistor |
| ratio | Ratio between a modified case and a base case |

| | |
|---|---|
| ref | Reference value |
| surf | Surface |
| s | Fin spacing |
| shield | Shield |
| side | Side of the heat sink |
| structure | Heat sink structure |
| surr | Surrounding temperature |
| top | Top surface of the heat sink |
| u | Unshielded |
| unshielded | Unshielded |

# 1. Introduction

This chapter is divided into five sections; the first section, section 1.1, discusses the increase in mobile communications, the role of wireless devices and the thermal challenges associated with these devices, and highlights the function of the Remote Radio Head (RRH). Section 1.2 investigates enhancements to natural convection for heat sinks with unique geometric features. Section 1.3 presents a review of radiation from finned heat sinks, section 1.4 defines the objectives of this investigation, and the final section, 1.5, presents a brief overview of the thesis structure.

## 1.1. Remote Radio Heads

In 2012, mobile data traffic was nearly twelve times the scale of the entire global Internet traffic in 2000; this dramatic increase requires operators to maximise the performance of remotely deployed wireless devices, such as RRHs (Cisco Systems, 2013). This increase in mobile data traffic is in the process of exploding from 2012 to 2017 by doubling in size each year as more people adopt, and utilise, smartphones (Ericsson, 2016). Smartphones, tablets, laptops and gaming devices are set to increase from roughly 6 billion devices in 2012 to 10 billion devices by 2017. Figure 1.1 illustrates this yearly growth and indicates that single mobile connected devices (such as tablets) will generate more traffic in 2017 than the entire mobile internet traffic in 2012. This expansion in mobile data traffic is facilitated by an increased complexity and functionality of wireless devices found in base stations.

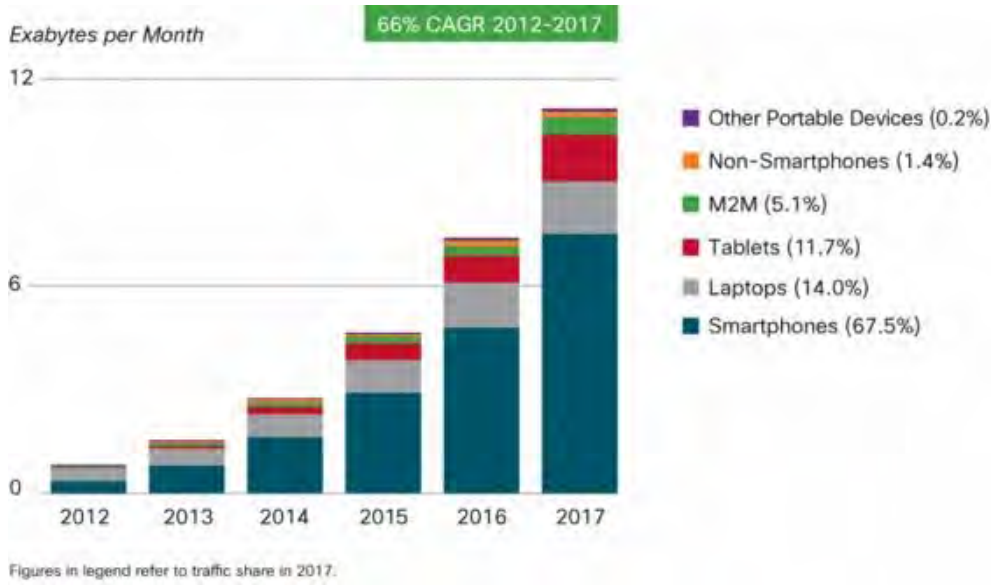


**Figure 1.1: Predicted data usage from mobile connected devices from 2012 to 2017 (Cisco Systems, 2013)**

Figure 1.2 shows the arrangement of a typical base station with a tower mounted RRH: a passive antenna delivering and receiving signals from the RRH via coaxial cables and a ground station featuring channel cards connected to the RRH via fiber optic cable (Commscope, 2012). A channel card is required for each frequency, and this consists of an RF power amplifier and conversion for transmission and reception (Kumar, 2014). The RRH consists of a transmitter containing a high power amplifier, a receiver that receives and amplifies radio waves sent from mobile stations, a base station interface, and other features (Asaina *et al.,* 2010). It greatly reduces the carriers' requirement for site resources, reduces feeder line loss and improves the effect of coverage (Texas Instruments, 2011). RRHs are being deployed to address the explosive growth in mobile data by increasing capacity and reducing cost (Ghosh *et al.*, 2012).


**Figure 1.2: RRH base station configurations (Commscope, 2012)**

RRHs are installed to improve coverage in urban environments and increase service to rural areas. RRHs are frequently positioned on radio base stations on masts, towers and buildings in potentially harsh environmental conditions. RRHs can feature high levels of heat dissipation, and can operate in harsh atmospheric conditions with ambient temperatures as high as 55 ℃ and wind speeds as low as $0ms^{-1}$ during periods of peak solar loading (Kim *et al.*, 2013). The RF power amplifier transistors in the RRH can represent up to 75% of the total RRH heat dissipation while the other components typically dissipate ~25 % but are limited in temperature (Zapach, 2009). It is also desirable to use a natural convection heat sink due to its fan less thermal design as fans produce acoustic noise and are susceptible to failure (Zapach, 2009). A representative RRH featuring a natural convection heat sink is shown in figure 1.3.

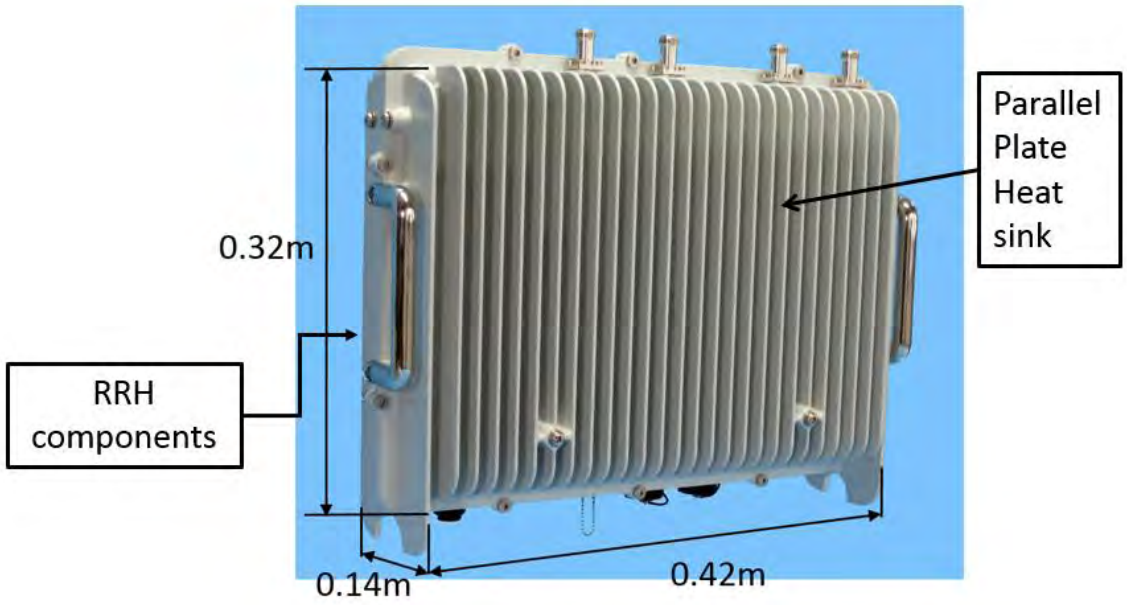


Figure 1.3: A representative RRH heat sink (Sumitomo Electric, 2012)

Natural convection is a commonly used technique to achieve unassisted heat transfer with applications in areas such as the nuclear industry, telecommunications industry and in solar energy. This thesis focuses on natural convection for remotely deployed wireless devices in the telecommunications industry, in particular RRHs.

## 1.2. Enhancements to Natural Convection

This section discusses the enhancements to a natural convection heat sink (shown in figure 1.4) and is split into four subsections. The first subsection presents a review of natural convection heat sinks with unique fin arrangements. Subsection 1.2.2 covers the use of the chimney effect to augment natural convection for flat plates and heat sinks. Subsection 1.2.3 provides a review of solar shroud and environmental considerations for a specific urban location at the hottest time of the year (Kuwait in Summer). The last subsection provides conclusions of the enhancements to natural convection.

Figure 1.4: A natural convection heat sink (Fischer Elektronic, 2016)

### 1.2.1. Modified Heat Sink

There have been numerous enhancements to natural convection heat sinks varying from perforated fins to pin fins embedded in the base plate. Iyengar and Bar-Cohen (1998) investigated vertical pin fin, plate fin and triangular fin heat sinks. They found that triangular fin heat sinks are superior to the pin fin and plate fin heat sinks, however, the pin fin was the most volumetrically efficient of the three. This makes pin fin heat sinks useful for applications with weight and material cost restrictions, however they are more costly to produce. Sparrow and Prakash (1980) performed a 2D numerical analysis to enhance heat transfer via the use of a staggered array of discrete vertical plates by reducing the boundary layer thickness to obtain higher heat transfer coefficients. Guglielmini *et al.* (1987) investigated natural convection and radiation on staggered vertical fins of finite length and thickness connected to an isothermal base plate. They found that staggered fins had a higher thermal performance over a non-staggered fin arrangement. Ledezma and Bejan (1997) optimised the geometric arrangement of staggered vertical plates in a fixed volume, experimentally and numerically, with the use of four parameters: the spacing between two adjacent rows, the number of plates mounted in one row of length, the plate height, and the stagger parameter. They found that staggered fins can increase the heat removed per surface area by 15 percent in comparison to a non-staggered array. Praught (1982) investigated the use of straight fins inclined at various angles to the vertical in order to increase the heat transfer performance. It was noted that as the length-to-height aspect ratio of the heat sink decreases, the heat transfer increases. A number of heat transfer enhancements involving modified heat sinks require expensive manufacturing techniques to implement new geometric designs, however, the use of fins separated with an air gap can provide a cost effective solution without altering the simplistic design of a parallel plate heat sink. This thesis will examine the effect of a vertical parallel plate natural convection heat sink, employing an air gap, on heat transfer.

### 1.2.2. Chimney Structure

The chimney effect occurs when air is hotter inside a chimney structure, than outside, causing a density driven flow. This results in cooler air being drawn in from an inlet at the base. A heat sink with and without a chimney is shown in figure 1.5. The use of a chimney structure to enhance flow is not uncommon; one of the earliest works by Moore (1973) investigated a natural draft heat exchanger system for large dry cooling towers. Marsters (1975) investigated experimentally the influence of a vertical chimney

in natural convection on a cylinder in air, water and Freon 113. Marsters investigated the change in heat transfer by varying the location of the cylinder from the inlet, the wall spacing and wall height to wall width. Marsters also found that a chimney structure enhanced heat transfer characteristics provided the wall height to wall width did not exceed 28. It was also noted that the location of the cylinder from the inlet of the chimney was of no apparent significance when the cylinder length is significantly larger than the cylinder diameter.

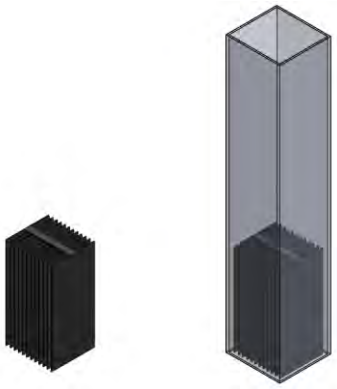

**Figure 1.5: An unshielded parallel plate heat sink (left) and a chimney enhanced parallel plate heat sink (right)**

Oosthuizen (1984) investigated, through numerical simulation, a heated parallel plate with adiabatic extensions. An increased flow rate provided a 50% increase in the heat transfer from the heated section with long adiabatic extensions. Lee (1994) numerically investigated laminar natural convection for separate cases with an unheated entry and unheated exit as shown in figure 1.6. Lee and Yan (1994) investigated laminar natural convection for an unheated entry and unheated exit with a heated middle section. They found the induced volumetric flow rate increased when the unheated entry length decreased.

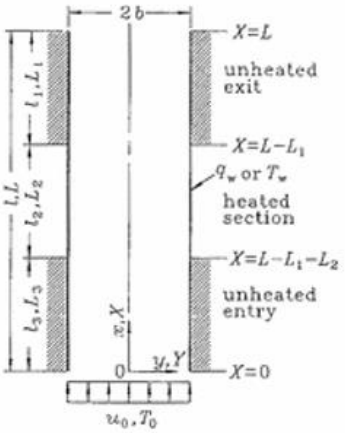


**Figure 1.6: Partially heated vertical parallel plates (Lee & Yan, 1994)**

Haaland and Sparrow (1983) investigated the channel plume in a parallel walled chimney; identical mass flows were found for two different sources, a line and a planar source, placed at the inlet of a tall, narrow channel. Asako *et al.* (1990) numerically modelled a vertical heated tube attached to a chimney of different diameter. The optimum diameter of the chimney was 1.4 to 2.7 times the diameter of the heated tube, depending on geometry, to maximise removal of heat. At this optimum diameter of the chimney, 250% more heat was removed when compared to a heated tube without a chimney.

La Pica *et al.* (1993) experimentally investigated the use of a vertical air channel and created an empirical correlation for the Nusselt number and Reynolds number which were a function of the channel Rayleigh number. Naylor and Tarasuk investigated, numerically (1993a) and experimentally (1993b), a divided vertical channel with heated walls on the chimney and a heated dividing plate. The position of the divided plate, relative to the inlet, severely affected the heat transfer rate at lower Rayleigh numbers; a contradiction of the findings reported by Marsters (1975). Marsters used two cylinder heights, the initial height and inverting the setup to create another configuration, however, the initial height was in close proximity to the midpoint of the experimental rig, which the author treated as a negligible change to the heat transfer. The average Nusselt number for a plate at the inlet was nearly double the average Nusselt number for a plate located at the exit. Straatman *et al.* (1993) investigated, experimentally and numerically, the use of adiabatic extensions, with varied length and width, to enhance heat transfer. An enhancement of up to 250 % in the Nusselt number was obtained for low modified channel Rayleigh number. A Nusselt number correlation was proposed based on modified channel Rayleigh number and the channel width.

Fischer *et al.* (1997) created an analytical solution for a natural convection draft heat sink system, based partly on the experimental work of Straatman *et al.* (1993). A porosity term was used to capture effects from a wider chimney and to account for the potential reduction in mean velocity at the exit and the mean channel velocity. Fischer *at al.* (1997) found that a reduction in heat sink height can be compensated by the higher local heat transfer rates produced by the chimney effect. This is achieved by a large temperature (and thus density) difference between the fluid inside and outside the chimney. Fischer and Torrance (1999) experimentally verified this analytical solution and found a decrease in heat transfer due to cold inlet flow; the experimental setup can be seen in figure 1.7.

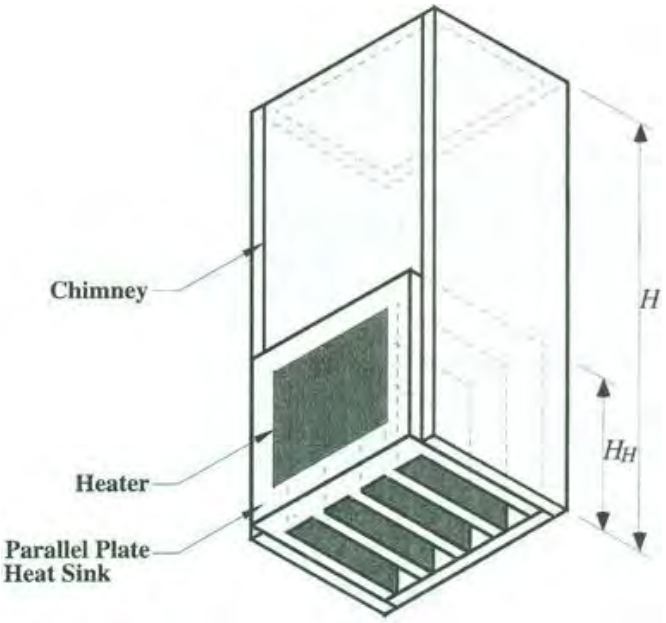


Figure 1.7: An isometric view of the chimney and heat sink (Fisher & Torrance, 1999)

Thrasher *et al.* (2000) showed that the analytical solution of Fischer and Torrance (1999) provided reasonable agreement when applied to pin fin heat sinks. Andreozzi *et al.* (2002) investigated the use of a partially heated parallel plate channel. They found the mass flow rate varied proportionally to the heated length and the aspect ratio. The authors also noted the infrequency of literature pertaining to chimneys and/or auxiliary added plates. Vermeersch *et al.* (2008) found that the thermal resistance of a transistor fixed on a fin in a cylindrical chimney improved thermal resistance by 10 % compared to a chimney-less setup. Rajkumar *et al.* (2013) investigated, experimentally and numerically, the use of fixed isoflux planar heat sources in a vertical channel; the stream-wise height ratio, a dimensionless parameter based on the plate height and channel length, was found to have a minimal influence on the Nusselt number. These authors also noted that heat transfer studies on multiple heat sources placed independently one above the other in a tandem, or segregated, arrangement with wall confinement are scarce (Rajkumar *et al.*, 2013). This provides the basis for this thesis to utilise an air gap, as investigated in section 1.2.1. This thesis will investigate the use of multiple heat sources in a segregated arrangement in a chimney structure to enhance the heat transfer from vertical natural convection heat sinks.

### 1.2.3. Solar Shroud

A shroud, or a solar absorbing chimney, provides passive solar cooling to reduce temperature (Bacharoudis *et al.*, 2007). Agonafer *et al.* (2010) have examined the influence of vent configurations on the solar shroud (or shield) of a high powered radio

control unit. Solar shields have also been investigated for a range of applications in harsh environments: for buildings, by Amers (2006); and for recording weather station data, by Hubbard *et al.* (2001). In other works, Mariam *et al.* (2009) and Marongiu *et al.* (1998) have assessed the thermal considerations for outdoor telecommunications cabinets. Of particular relevance to the work presented in this thesis, Hawley and Palaszewski (2011) investigated the thermal behaviour of outdoor cellular electronics for a hot location in the United States (Yuma, Arizona), and stated the need to determine appropriate environmental conditions for thermal models that underpin reliability estimation methodologies. They also concluded that inclusion of average wind speed at maximum solar load can reduce board temperatures by 9-11℃. It is clear that the judicious use of realistic environmental data as boundary conditions for the thermal analysis of outdoor electronics is advisable, in order to improve design practice.

With reference to environmental conditions, Hawley and Palazewski (2011) determined that in order to represent electronic devices in an environmentally defined worst case condition, appropriate environmental parameters from a city in a hot dry climate is required. Nasrallaha *et al.* (2004) investigated Kuwait, a location on the Arabian Peninsula, which has a harsh climate with warm seasons during May-August that feature an average air temperature range of 31.6 to 37.3 ℃ (1958 to 2000). Al-Fahed *et al.* (1997) reported ambient temperatures exceeding 50℃ during the summer months. Al-Fahed *et al.* (1997) noted that the data for July demonstrates some of the highest global average maximum, minimum and mean temperatures. Telcordia Technologies (2009) recently released standard GR-487 which defines the testing environment for electronic equipment; specifically, the model must be tested under a 25 ℃ increase, less than 0.1 $ms^{-1}$ wind, 753 $Wm^{-2}$ solar load applied to 100 % on the top surface area and 50 % on the total vertical surface area. Agonafer *et al.* (2010) in their investigation of a solar shroud using CFD, utilized a worst case environmental condition of a 55 ℃ ambient temperature, 0 $ms^{-1}$ wind speed, and the solar loading defined in accordance with GR-487.

### 1.2.4. Conclusions

In this section, research into enhancements to a natural convection heat sink using a modified heat sink, chimneys and solar shrouds are presented. A number of modified heat sinks require expensive manufacturing techniques however, the use of staggered fins heat sinks produce higher heat transfer coefficients, as reported by Sparrow and Prakash (1980), without being prohibitively expensive. The additions of chimneys,

presented in section 1.2.2, can enhance heat transfer by up to 250 %, as reported by Straatman *et al.* (1993). Solar shrouds, discussed in section 2.1 are utilised to provide passive solar cooling as noted by Bacharoudis *et al.* (2007), however the use of multiple independently placed heat sinks in a chimney structure is rare, as noted by Rajkumar *et al.* (2013). For an RRH, the power amplifiers typically dissipate ~75 % of the total heat, while the other components typically dissipate ~25 % but are limited in air operational temperature. This suggests a possibility to splitting these two distinct heat sources into a staggered array within a chimney structure, with the temperature sensitive components at the base and the high power dissipating component (power amplifiers) at the top. Kuwait City typically has the highest design temperature in the world which could be used to provide a baseline for environmental parameters. The preceding literature review indicates the potential for enhanced cooling for natural convection heat sinks using an independently staggered heat sink structure.

## 1.3. Radiation

Radiation from finned heat sinks can account for ~25 % of total heat transfer. Rea and West (1976) proposed a calculation for radiation heat transfer based upon an effective emissivity, which could be greater than unity. Ellison (1979) proposed to use the emissivity of the object alongside a view factor to calculate radiation. Shabany (2008) noted that no explicit analytical formulation existed for effective emissivity or view factor and proposed the correlation to accurately predict the view factor of a plate fin heat sink given in section 3.2 (Shabany, 2010).

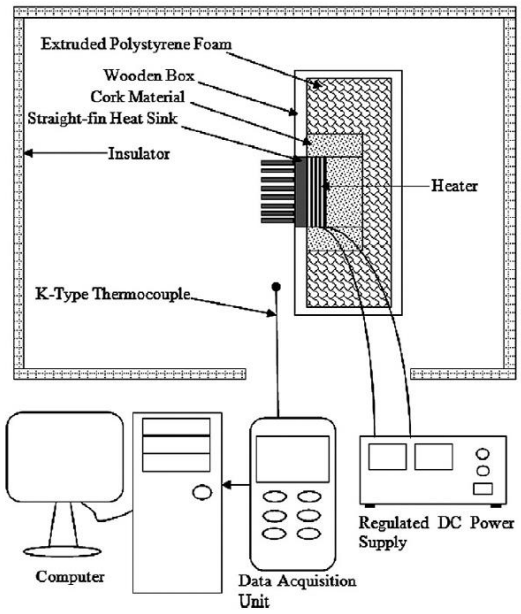


**Figure 1.8: Schematic of experimental apparatus to calculate the view factor (Khor, et al., 2010)**

Khor *et al.* (2010) experimentally investigated the correlation, proposed by Shabany, for thermal radiation and view factor of plate fin heat sinks. A schematic of the experimental apparatus used by Khor *et al.* is shown in figure 1.8. The findings indicate that the equations proposed by Shabany can be accurately used to predict radiation heat transfer within 3 %.

## 1.4. Objectives

The literature review indicates the need for enhanced cooling techniques for RRHs. There exists the potential to utilize a solar shield and a segregated structure, shown in figure 1.9, to enhance heat transfer for an RRH. This thesis aims to investigate the natural convection heat transfer from a heat sink representative of an RRH for a range of different environmental, geometrical and operational conditions.

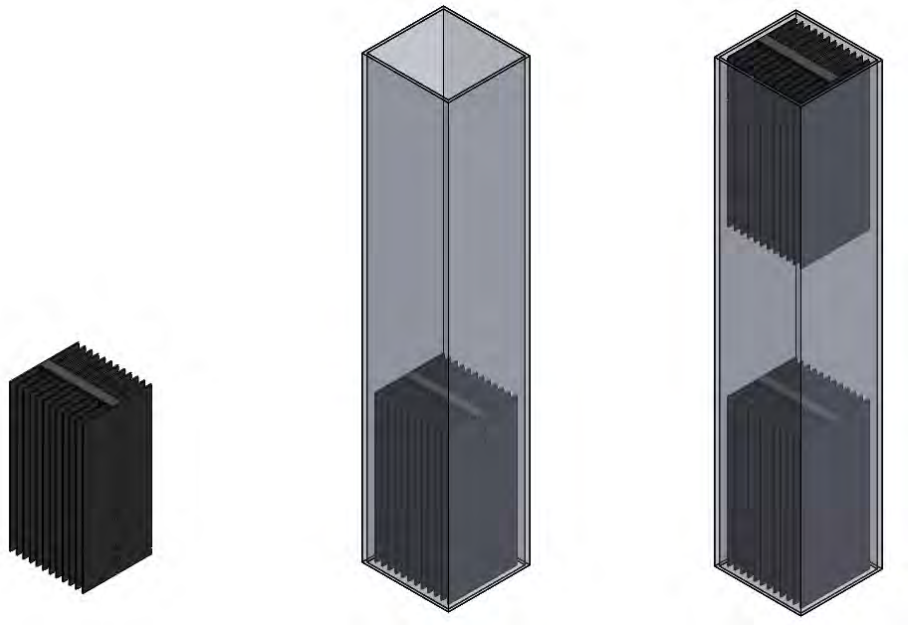

**Figure 1.9: The three different configurations under consideration in this thesis; unshielded (left), shielded (centre) and segregated structure (right)**

### 1.4.1. Solar Shield

Outdoor electronic equipment is subject to strict industry standards defined in Telcordia GR-487. This states that solar irradiation of 754 $Wm^{-2}$ should be imposed on the top with 377 $Wm^{-2}$ on the side and front of the sink, with an ambient air temperature of 55 °C and 0 $ms^{-1}$ wind speed. In order to investigate the severity of the requirements in Telcordia GR-487, the objective of this thesis is to:

- Compare the results from a numerically modelled heat sink with and without a solar shield subject to Telcordia GR-487 and in an environmentally defined worst case condition during the hottest day in a populated city. The orientation

should maximise the projected area of the heat sink exposed to the sun during periods of peak solar irradiation and high ambient temperature.

- Modify the solar shield to determine the impact of shield length and location of the heat sink within the shield.

### 1.4.2. Segregated Structure

For an RRH, the power amplifiers typically dissipate ~75 % of the total heat, while the other components typically dissipate ~25 % but are limited in temperature. There exists the potential to represent the RRH as two distinct heat sinks, a primary heat sink containing temperature sensitive components and a secondary heat sink containing the non-temperature sensitive power amplifiers. For the analysis of the segregated structure, the objective of this thesis is to:

- Examine a primary heat sink, shielded and unshielded, limited to a 25 °C above ambient, representative of the temperature sensitive components and compare the Nusselt numbers.
- Investigate the impact of adding a secondary heat sink to the shielded structure capable of a 65 °C above ambient. Compare the Nusselt number of the unshielded primary heat sink to the Nusselt number of the primary heat sink in this segregated structure.
- Determine the impact of the vertical location of the secondary heat sink to maximise the heat transfer.
- Modify the secondary heat sink by increasing and decreasing the spacing between fins and, as a result, the number of fins on the heat sink.

## 1.5. Thesis Structure

The remainder of this thesis has been split into six main chapters. Chapter 2 presents the heat sinks, representative of a RRH, and shields under investigation in this thesis. Chapter 3 details the relations, from literature, used to estimate radiative and convective heat transfer. Chapter 4 describes the theory and procedure for compiling the numerical analysis. Chapter 5 details the apparatus and procedure for quantifying the experimental results. Chapter 6 discusses the results obtained from the numerical and experimental investigations, and Chapter 7 presents the conclusions and recommendations from this thesis.

# 2. RRH Structures

This chapter presents the heat sinks, representative of a RRH, and corresponding structures under investigation in this thesis and is split into three sections. The first section details the heat sink and solar shield used to numerically investigate the environmental conditions applied by the industry standard and a representative worst case condition. The second section presents the heat sinks, primary and secondary, and shield used to investigate, numerically and experimentally, a segregated structure. The third section provides a summary of this chapter. The structures investigated in this chapter were deemed sufficient to consider in isolation of the rest of the RRH, as the heat sink is typically the predominant path for heat to flow from internal components to ambient.

## 2.1. Solar Shield

In this section, there are two subsections; solar shield geometric properties and environmental properties. The first subsection discusses environmental conditions used to model a harsh climate, where high ambient temperatures and solar loading impose significant thermal loads on RRHs, and the second subsection details the physical properties of an RRH typically deployed in a harsh environmental area.

### 2.1.1. Environmental Properties

In order to represent a remote radio head in an environmentally defined worst case condition, appropriate environmental parameters from a city in a hot climate are required (Hawley & Palaszewski, 2011). Kuwait City has the highest design temperature in the world, and this location was used to provide a baseline for environmental parameters. The heat sink was vertically aligned and facing in a south-westerly orientation during the hottest day in Kuwait City in July of 2011. This orientation was chosen to maximise the projected area of the heat sink exposed to the sun during periods of peak solar irradiation and high ambient temperature (12:00 to 16:00). Solar irradiation and position (azimuthal and altitude angle) was determined using a solar calculator (Brackenridge, 2011).

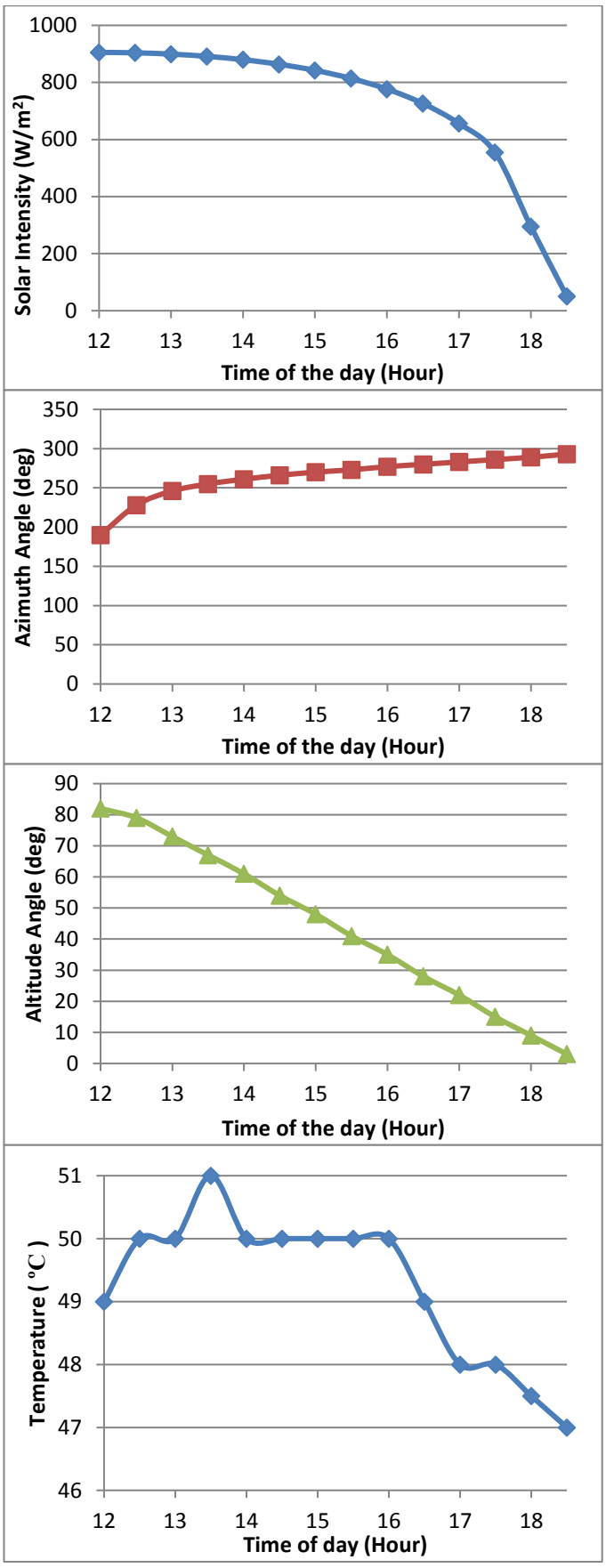


**Figure 2.1: Solar intensity, azimuth angle, altitude angle (Brackenridge, 2011) and ambient temperature (Weather Underground, Inc., 2011), as a function of time of day in Kuwait on the 15th of July 2011**

The thermal behaviour of the heat sink was modelled from noon to sunset as ambient air temperature typically reaches a maximum after the period of peak solar intensity. Weather data could have been obtained from the American Society of Heating, Refrigerating, and Air-Conditioning Engineers (ASHRAE) in their handbook (ASHRAE, 2009) or from the World Meteorological Organization (WMO), however, this utilised data from Kuwait International Airport (WMO: 405820). Kuwait International Airport is located in a sparsely populated area in comparison to the main street in Kuwait City where space is at a premium and capacity can be strained. To create a practical environmentally defined condition ambient temperatures were taken at 30 minute intervals from an online database of national weather stations from the National Oceanic and Atmospheric Administration and National Aviation Authorities along with private weather stations for Kuwait City (Weather Underground, Inc., 2011), with any missing data being the average of 30 minutes before and after the missing data point. Solar conditions and ambient temperature are shown in figure 2.1

This environmentally defined condition was compared with an industry standard, Telcordia GR-487, which has been identified by Hawley & Palaszewski (2011) as the industry standard . Solar irradiation of 754 $Wm^{-2}$ was imposed on the top with 377 $Wm^{-2}$ on the side and front of the sink, with an ambient air temperature of 55 ℃ and 0 $ms^{-1}$ wind speed. The results of this numerical study are presented in section 6.1.

### 2.1.2. Solar Shield Geometric Properties

The heat sink and solar shield, shown figure 2.2, is a typical extrusion grade aluminium heat sink, due to its low density and high thermal conductivity (180 $Wm^{-1}.K^{-1}$). Dimensions of the heat sink were 300 mm length, 150 mm width, 60 mm height and a base thickness of 5mm, shown in table 2.1. A fin thickness of ~2.5 mm was assumed, which is typical of extrusion grade structures. In the analysis presented in this thesis, a set temperature of 80 ℃, the limit of temperature sensitive component (25 ℃ over ambient), and the heat dissipation from the sink was evaluated as a measure of thermal performance. A fixed heat load was not applied, as this would have resulted in non-constant sink temperatures and a wide range of optimum fin spacing. Established empirical relations for parallel plates (see equation 3.8 in section 3.1) were used to determine the optimum fin spacing for the heat sink, which was found to be ~9.75 mm.

The solar shield was also formed from aluminium, and it featured a length of 300 mm, width of 170 mm, thickness of 5 mm, and clearance of 5 mm from the surfaces of the sink for its default geometry. The shield did not cover the top and bottom of the heat sink, in order to allow air to flow freely through the heat sink. As part of this thesis, the shield length was increased from 300 mm to 900 mm in steps of 200 mm. For a shield length of 900 mm, the vertical position of the heat sink within the shield was varied from the base to the top in steps of 100 mm in order to assess the influence of the chimney flow effect. Finally, to investigate the effect of clearance, the spacing between the shield and the surfaces of the heat sink was varied from 2 mm to 10 mm in steps of 2 mm for a shield height of 300 mm.

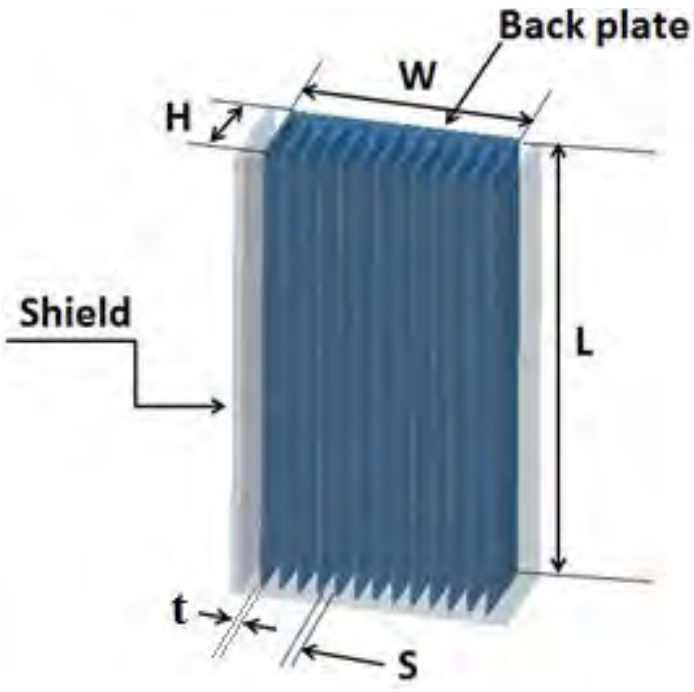


**Figure 2.2: The heat sink and solar shield combination of a representative outdoor electronics device modelled in Star-CCM+**

**Table 2.1: Geometric properties of the heat sink and segregated structure**

| Symbol | Meaning | Dimensions |
|---|---|---|
| *W* | Width | 150.0 mm |
| *L* | Length | 300.0 mm |
| *H* | Height | 60.0 mm |
| N | Number of fins | 13 |
| t | Fin thickness | 2.5 mm |
| B | Base plate thickness | 5.0 mm |

| | | |
|---|---|---|
| S | Fin spacing | 9.75 mm |
| $L_{shield}$ | Length of the solar shield | 300 mm |
| $W_{shield}$ | Width of the solar shield | 170 mm |
| $t_{shield}$ | Thickness of the solar shield | 5 mm |
| $H_{shield}$ | Height of the solar shield | 70 mm |

Standard properties of air at sea level and an ambient temperature of 55 ºC were assumed and, to represent radiation heat transfer, extrusion grade aluminium was assigned an emissivity of 0.95 and an effective solar absorptivity of 0.25 – properties typical of a white painted surface (Shabany, 2010).

## 2.2. Segregated Structure

The configuration under investigation in this subsection is a set of two aluminium heat sinks, shown in figure 2.3 with dimensions given in table 2.2, and the shielded and segregated structure configurations shown in figure 2.4.

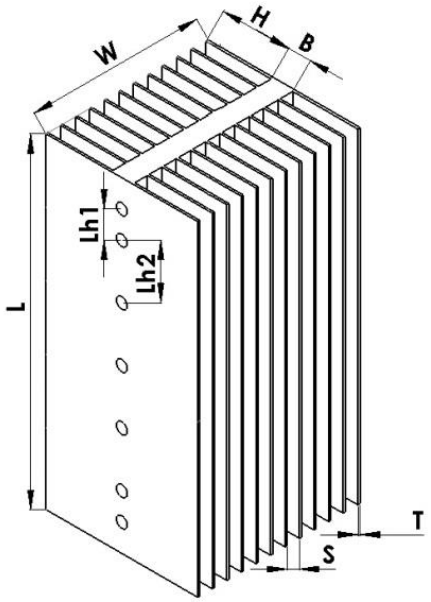


Figure 2.3: Geometric properties of a double sided heat sink

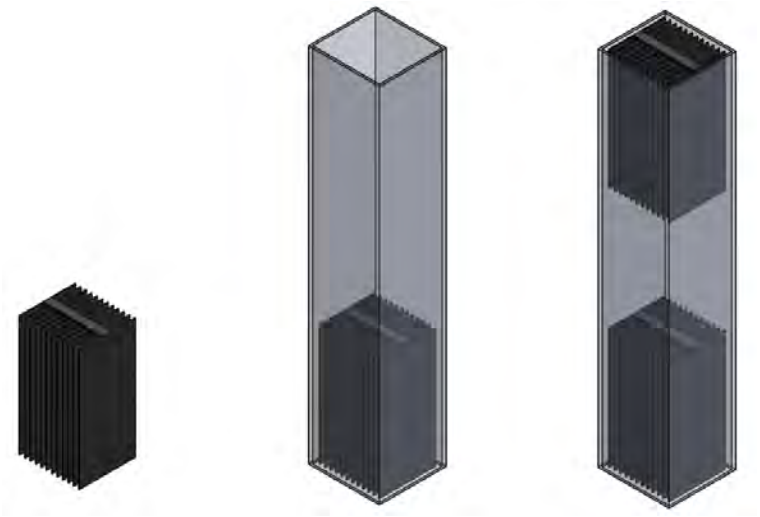

Figure 2.4: The three different configurations under consideration in this thesis; unshielded (left), shielded (centre) and segregated structure (right)

Table 2.2: Geometric properties of the heat sink and segregated structure

| Symbol | Meaning | Dimensions |
|---|---|---|
| $W$ | Width | 149.5 mm |
| $L$ | Length | 300.0 mm |
| $H$ | Height | 60.0 mm |
| $L_{shield}$ | Length of the shield | 900.0 mm |
| $L_{h1}$ | Distance between cartridge heaters | 25.0 mm |
| N | Number of fins | 24 |
| $t$ | Fin thickness | 1.9 mm |
| $B$ | Base plate thickness | 20.0 mm |
| $S$ | Fin spacing | 11.5 mm |
| $W_{shield}$ | Width of the shield | 161.5 mm |
| $L_{h2}$ | Distance between cartridge heaters | 50.0 mm |

The heat sink, shown in figure 2.3, was modelled as an aluminium 6082T6 heat sink, with a density of 2700 kg $m^{-3}$, thermal conductivity of 180 W $m^{-1}$ $K^{-1}$ and an emissivity of 0.97 as acquired in section 5.3. The shielding material was made from polycarbonate with an emissivity of 0.95, as obtained in section 5.3, a thermal conductivity of 0.19 W $m^{-1}$ $K^{-1}$ and a density of 1200 kg $m^{-3}$ (Brydson, 2000). Detailed geometries of the heat sink and shielding material are given in chapter 5.1.

In the analysis presented in this thesis, a set temperature difference between the heat sink base plate temperature ($T_p$) and ambient is imposed on heat source locations, as shown as $L_{h1}$ and $L_{h2}$ in figure 2.3 and given in table 2.3. Ambient temperature are lower than those discussed in section 1.2, for Telcordia GR-487, as thermal properties are easily obtainable and natural convection is significantly impacted by temperature difference. Firstly, a single heat sink was numerically modelled in isolation and compared to experimental data and established theory. The heat sink was then placed at the base of a shield, 900 mm in length, and examined, experimentally and numerically, using the ambient temperatures and temperature difference which are listed in table 2.3, the values were obtained experimentally, in order to provide a direct comparison to the numerical and experimental data. An unheated secondary heat sink was then added to the top of the shielded structure, as shown in figure 2.4. The results of this numerical and experimental study are presented in section 6.2.

**Table 2.3: Ambient and temperature difference for an unshielded, shielded and secondary heat sink with no heat**

| **Unshielded** | | **Shielded** | | **Secondary No Heat** | |
|---|---|---|---|---|---|
| **Ambient (°C)** | $T_p - T_\infty$ (°C) | **Ambient (°C)** | $T_p - T_\infty$ (°C) | **Ambient (°C)** | $T_p - T_\infty$ (°C) |
| 19.2 | 5.1 | 17.0 | 5.1 | 18.0 | 5.1 |
| 19.1 | 10.1 | 17.1 | 10.1 | 18.7 | 10.0 |
| 19.1 | 15.0 | 17.0 | 15.0 | 18.8 | 15.0 |
| 19.2 | 20.0 | 16.3 | 20.0 | 19.2 | 20.0 |
| 19.3 | 25.0 | 16.8 | 25.0 | 19.2 | 24.9 |
| 19.4 | 34.9 | 17.2 | 34.9 | 16.4 | 34.8 |
| 19.4 | 44.8 | 17.6 | 44.8 | 19.2 | 44.8 |
| 20.3 | 54.8 | 18.1 | 54.7 | 17.6 | 54.8 |
| 20.5 | 64.7 | 18.4 | 64.5 | 18.7 | 65.4 |

A segregated structure with a heated secondary heat sink was then modelled, experimentally and numerically, varying the gap distance between the primary and secondary heat sinks as shown in figure 2.5. The secondary heat sink had a temperature difference between the heat sink base plate temperature ($T_{sec}$) and ambient temperature given in table 2.4 which was obtained experimentally. The segregated structure was numerically modelled with a gap distance of 0 mm up to 300 mm in steps of 50 mm;

additionally a gap distance of 5 mm was also evaluated as this was the closest point to experimentally verify. At a gap distance of 0mm, both heat sinks were in physical contact, however, they were not permitted to conduct heat directly to each other in the numerical simulations. The primary heat sink was kept at a constant temperature difference of 25 ℃ above ambient as outlined in chapter 5.5.

Finally, based on the results from the location of the heated secondary heat sink, the number of fins on the secondary heat sink was varied numerically to optimise the heat removed from the primary heat sink. The fin thickness was kept constant at 1.9mm as given in table 2.2, while the number of fins was varied from 2, in steps of 2, up to 14 fins; additionally configurations were tested at 7, 13 and 15 fins. The thermal properties were taken at an ambient temperature of 19.5 ℃, a primary heat sink temperature of 25 ℃ above ambient and a secondary heat sink temperature of 64.4 ℃.

**Table 2.4: Boundary conditions of a heated secondary heat sink in a segregated structure**

| **Secondary Heat Sink** | | |
|---|---|---|
| **Gap Distance (mm)** | **Ambient (℃)** | $T_{sec} - T_{\infty}$ (℃) |
| 0 | 19.5 | 64.4 |
| 5 | 14.8 | 64.3 |
| 50 | 19.5 | 64.4 |
| 100 | 20.8 | 64.2 |
| 150 | 19.5 | 64.4 |
| 200 | 15.4 | 64.3 |
| 250 | 19.5 | 64.4 |
| 300 | 19.5 | 64.4 |

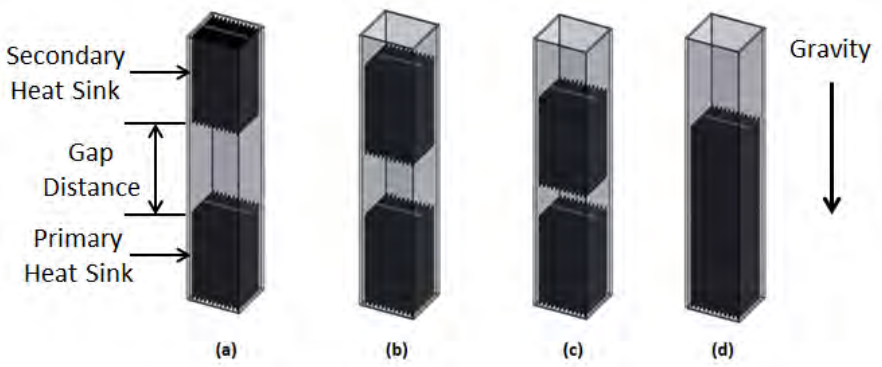


**Figure 2.5: Segregated heat sink structures with varied heat sink gap; (a) 300mm (b) 200mm, (c) 100mm and (d) 5mm**

## 2.3. Summary

This chapter presents the numerical and experimental structures investigated in this thesis. For a solar shield, a heat sink, optimised at Telcordia GR487, was outlined and a solar shield was used to compare the environmental properties applied by Telcordia GR487 to representative worst case condition. A segregated structure was detailed with the different parameters under investigation in this thesis. The next chapter will discuss the theory utilised in this thesis to analytically model the structures outlined in this chapter.

# 3. Theory

This chapter presents the relations, from established literature, used to calculate the convective and radiative heat transfer from a single isothermal heat sink and to estimate the radiation heat transfer of a secondary segregated structure. This chapter is split into three sections: the first, 3.1, presents equations to determine the natural convection heat dissipation for an unshielded heat sink using this optimum spacing. The next section, 3.2, presents the radiative heat transfer for an isothermal heat sink with assumptions used to estimate the radiation from a vertical parallel plate heat sink in a segregated structure; and, finally, the last section, 3.3, presents conclusions.

## 3.1. Natural Convection

The fundamentals for natural convection parallel plates are well documented, with equations to determine the optimum spacing of parallel plates (Bar-Cohen & Rohsenow, 1984) and how to modify this optimum spacing for a parallel plate heat sink (Malhammer, 1987).

Five dimensionless parameters are used here to quantify natural convection heat transfer: the Prandtl number (Pr), Grashof number (Gr), Nusselt number (Nu), Rayleigh number (Ra) and Elenbaas number (El). The Prandtl number of a fluid is its ratio of momentum to thermal diffusivities:

$$Pr = \frac{momentum\ diffusivity}{thermal\ diffusivity} = \frac{c_p \mu}{k_f} \qquad 3.1$$

Where $c_p$ is the specific heat capacity, $\mu$ is the dynamic viscosity and $k_f$ is the thermal conductivity.

The Grashof number is the ratio of buoyancy forces to viscous forces acting on the fluid and is given in the following equation:

$$Gr_x = \frac{g\beta\left(T_{surf} - T_{\text{amb}}\right)x^3}{\nu^2} \qquad 3.2$$

Where $Gr_x$ is the Grashof number based on the characteristic length ($x$), $g$ is gravity, $\beta$ is the volumetric thermal expansion coefficient of the fluid, $\nu$ is the kinematic viscosity of the fluid, $T_{surf}$ is the surface temperature and $T_{\text{amb}}$ the ambient temperature.

The Rayleigh number ($Ra_x$), also based on a characteristic length, is the product of the Grashof number and the Prandtl number:

$$Ra_x = Gr_x Pr \quad 3.3$$

A derivative of the Rayleigh number, the Elenbaas number ($El$), is a geometrically modified Rayleigh number applicable to vertical parallel plates and heat sinks and is given in equation 3.4:

$$El = Ra_s \frac{S}{L} \quad 3.4$$

Where S is the plate-to-plate distance, and L is the length of the plate in the direction aligned to gravity.

The Nusselt number is the ratio of the convective and conductive heat transfer at the fluid surface interface:

$$Nu_x = \frac{convective\ heat\ transfer}{conductive\ heat\ transfer} = \frac{hx}{k_f} \quad 3.5$$

Where $Nu_x$ is the Nusselt number based on a characteristic length, $h$ the heat transfer coefficient and $k_f$ the thermal conductivity. The characteristic length is typically chosen as the boundary layer growth direction; for plates, this is the plate length (Incropera *et al.*, 2011).

Air properties for convection depend on the temperatures under investigation, so the film temperature is used to evaluate the air properties and is given in equation 3.6:

$$T_{film} = \frac{T_{surf} - T_{amb}}{2} \quad 3.6$$

The average Nusselt number ($\overline{Nu_s}$) for a heat sink is calculated according to equation 3.7:

$$\overline{Nu_s} = \frac{Q_{conv} S}{A_{hs}(T_{surf} - T_{amb})k_f} \quad 3.7$$

The average Nusselt number over the entire surface of the heat sink is calculated using the total heat removed by convection ($Q_{conv}$), and the entire heat sink area ($A_{hs}$) at a set base plate temperature above ambient temperature. Equation 3.7 is used to calculate the average Nusselt number from experimental data.

The total convective heat transfer for an unshielded heat sink, shown in figure 3.1 with the base highlighted in red and the fins highlighted in green, can be determined using equation 3.8 (Bar-Cohen & Rohsenow, 1984):

$$Q_{conv} = NQ_{fin} + h_{base}A_{base}(T_{surf} - T_{amb}) \quad 3.8$$

Where $Q_{conv}$ is the total heat removed by convection, N is the number of fins, $Q_{fin}$ is the heat dissipated in a single fin, $h_{base}$ is the heat transfer coefficient for the unfinned base area, calculated in equation 3.9, and $A_{base}$ is the area of the unfinned base shown in red in figure 3.1.

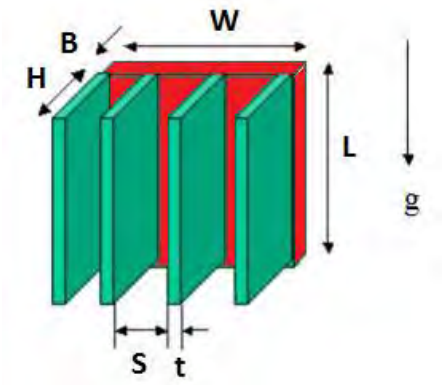


**Figure 3.1: A vertical parallel plate heat sink with the base highlighted in red and the fins highlighted in green**

The Nusselt number for the base plate ($Nu_{base}$) is calculated using the thermal conductivity of the air at the film temperature ($T_{film}$), the Rayleigh number, length of the heat sink and heat transfer coefficient for the base plate (Bar-Cohen & Rohsenow, 1984):

$$Nu_{base} = \frac{h_{base}L}{k_f} = 0.59\mathrm{Ra}_{\mathrm{L}}^{0.25} \quad 3.9$$

The heat removed by a convection from a single fin can be defined is calculated using equation 3.10:

$$Q_{fin} = h_{fin}A_{fin}(T_{surf} - T_{amb}) \quad 3.10$$

The heat removed by a convection from a single fin can be calculated using the heat transfer coefficient of the fin ($h_{fin}$), the finned area ($A_{fin}$) and the surface and ambient temperatures.

The Elenbaas number is named after Willem Elenbaas who was the first to present a comprehensive experimental investigation into the use of isothermal vertical parallel plates in natural convection (Elenbaas, 1942). However, analysis by various authors found at low plate-to-plate spacing, the heat losses calculated by Elenbaas were greater than the actual heat removed by natural convection and, for larger plate temperatures, thermal radiation was significant (Sparrow & Bahrami, 1980). Bar-Cohen and

Rohsenow (1984) further investigated the use of vertical isothermal parallel plates, shown in figure 3.2, and proposed a correlation for the average Nusselt number of the fins given in equation 3.11:

$$\overline{Nu}_s = \left[\frac{576}{(\eta_{fin}El)^2} + \frac{2.87}{(\eta_{fin}El)^{0.5}}\right]^{-0.5} = \frac{h_{fin}S}{k_f} \qquad 3.11$$

This correlation is an asymptotic solution for two distinct physical phenomena:

1. If the spacing is large, each isothermal vertical parallel plate acts as an isolated isothermal vertical flat plate $\left(\frac{576}{(\eta_{fin}El)^2}\right)$

2. A low spacing causes the thermal boundary layers of each flat plate to merge, reducing the performance of the plates $\left(\frac{2.87}{(\eta_{fin}El)^{0.5}}\right)$

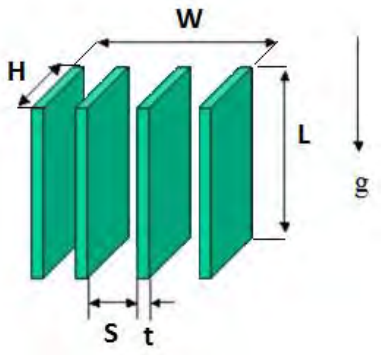


Figure 3.2: Vertical parallel plates

The average Nusselt number ($\overline{Nu}_s$), proposed by Bar-Cohen and Rohsenow (Bar-Cohen & Rohsenow, 1984), over the finned surface of the heat sink is calculated using the Elenbaas number defined in equations 3.4 and the convective fin efficiency ($\eta_{fin}$) defined in equation 3.12:

$$\eta_{fin} = \frac{\tanh(mH_c)}{mH_c} \qquad 3.12$$

The convective fin efficiency, used to account for temperature variations in the fins, is calculated from the fin parameter ($m$) calculated in equation 3.13, the corrected fin height ($H_c$) calculated using equation 3.14 (Shabany, 2010):

$$m = \left(\frac{2h_{fin}(t+W)}{k_{fin}tW}\right)^{0.5} \qquad 3.13$$

$$H_c = H + 0.5\frac{tW}{t+W} \quad 3.14$$

The fin parameter and the corrected fin height are defined using the fin height ($H$), fin thickness ($t$), heat sink width ($W$) and the heat transfer coefficient for the fin calculated using equation 3.11.

The optimum spacing is the point at which the boundary layers of two parallel plates merge at the exit, maximising the amount of parallel plates in a confined space. This is given in equation 3.15 (Bar-Cohen & Rohsenow, 1981):

$$S_{\text{opt}} = 2.71\left(\frac{Ra_L}{L^4}\right)^{-\frac{1}{4}} \quad 3.15$$

Malhammer (1987) built upon Bar-Cohen and Rohsenow's correlations, for multiple vertical isothermal parallel plates, by incorporating the effect of the base plate in order to allow these correlations to be utilised for non-isothermal vertical parallel plate heat sinks:

$$S = \frac{2HS_{opt}}{2H - S_{opt}} \quad 3.16$$

Where ($S_{opt}$) is the optimum spacing for vertical isothermal parallel plates as defined in equation 3.15 and S is the plate to plate spacing of a vertical parallel plate heat sink with a fin height ($H$).

In order to document the impact of the primary heat sink in a segregated structure, the Nusselt ratio is used in section 6.2. The Nusselt ratio is a comparison of the unshielded heat sink Nusselt number to a shielded or a segregated structure and is given in equation 3.17:

$$Nu_{ratio} = \frac{Nu_{structure}}{Nu_{unshielded}} \quad 3.17$$

Where $Nu_{ratio}$ is the Nusslt Number ratio, $Nu_{structure}$ is the Nusselt number of the structure under investigation and $Nu_{unshielded}$ is the Nusselt number of the unshielded heat sink.

The equations to determine the natural convection heat dissipation for an unshielded heat sink and the ability to compare a heat sink in different structures have been specified in this section. These equations do not consider the radiative heat transfer; this is given in the next section.

## 3.2. Radiation

This section is split into two subsections; the first subsection, 3.2.1, presents the radiation equations for an unshielded heat sink. The next subsection, 3.2.2, presents the radiation equations and assumptions for a shielded heat sink. The heat dissipated by radiation is calculated using these equations from established literature by Shabany (2008, 2010) and Khor *et al.* (2010) in order to isolate $Q_{conv}$ from the experimentally measured total heat dissipation.

### 3.2.1. Unshielded Heat Sink

Radiation for a parallel plate heat sink can account for 25% of total heat transfer (Rea & West, 1976). Equation 3.18 was used to calculate heat dissipated by radiation:

$$Q_{rad} = \eta_r\left(Q_{top} + Q_{bot} + Q_{side} + (\mathrm{N}-2)Q_{channel}\right) \qquad 3.18$$

The total heat removed by radiation ($Q_{rad}$) is calculated using the heat removed by radiation from the top ($Q_{top}$), bottom ($Q_{bot}$), side ($Q_{side}$) and channel ($Q_{channel}$) surfaces as shown in figure 3.3. N is the number of fins and $\eta_r$ accounts for the temperature variation in the fins and is calculated in equation 3.19.

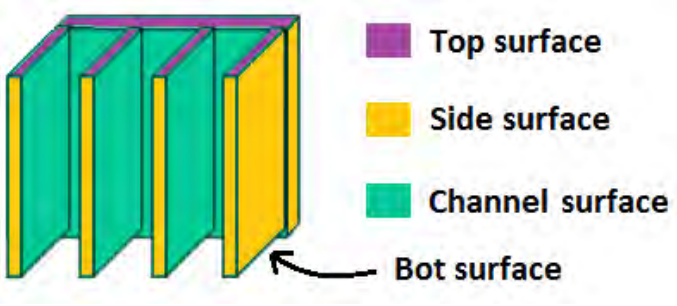


Figure 3.3: Radiation surfaces from a vertical parallel plate heat sink

The radiation heat sink efficiency is used to account for the temperature variation in the fins and can be calculated as follows:

$$\eta_r = 1 - \frac{NA_{fin}}{A_{hs}}\left(1 - \eta_f\right) \qquad 3.19$$

Where

$$A_{fin} = 2(L+t)H + Lt \qquad 3.20$$

$$\eta_f = \frac{\tanh\left[\left(H + \frac{t}{2}\right)\sqrt{\frac{2h_r(L+t)}{k_{hs}Lt}}\right]}{\left(H + \frac{t}{2}\right)\sqrt{\frac{2h_r(L+t)}{k_{hs}Lt}}} \qquad 3.21$$

The radiative heat sink fin efficiency ($\eta_f$), in equation 3.21, is a similar format to the convective heat sink fin efficiency in equation 3.12. It is the ratio of the fin radiative heat transfer rate over the heat transfer if the entire fin was at the base temperature. The radiative heat sink fin efficiency is calculated using the fin height, fin thickness, base thickness, heat sink width, length, the thermal conductivity ($k_{hs}$) of the heat sink, the heat sink ($A_{hs}$) and finned ($A_{fin}$) areas and the radiation heat transfer coefficient ($h_r$) which is given in equation 3.22:

$$h_r = \frac{Q_{top} + Q_{bot} + Q_{side} + (\mathrm{N}-2)Q_{channel}}{A_{hs}\left(T_{surf} - T_{amb}\right)} \qquad 3.22$$

The radiation heat transfer coefficient is calculated using the heat removed by radiation from the top, bottom, side and channel surfaces, the total heat sink area, and the surface and the ambient temperatures.

For an unshielded heat sink, the radiative heat removed for the top, bottom and side surfaces are calculated using the following equations:

$$Q_{top} = \sigma\varepsilon(HtN + BW)\left(T_{surf}^4 - T_{surr}^4\right) \qquad 3.23$$

$$Q_{bot} = \sigma\varepsilon(HtN + BW)\left(T_{surf}^4 - T_{surr}^4\right) \qquad 3.24$$

$$Q_{side} = \sigma\varepsilon(4H + 2B + tN)L\left(T_{surf}^4 - T_{surr}^4\right) \qquad 3.25$$

$$Q_{channel} = \sigma\hat{F}(S + 2H)L\left(T_{surf}^4 - T_{amb}^4\right) \qquad 3.26$$

The heat dissipated by radiation from the top, bottom, side and channel are calculated using the Stefan-Boltzmann constant ($\sigma$), the emissivity ($\varepsilon$) of the heat sink, the fin height, fin thickness, base thickness, heat sink width, length, number of fins, the surface and surrounding temperatures and $\hat{F}$, the exact view factor calculation given in equation 3.27 (Shabany, 2008):

$$\hat{F} = \frac{1}{\frac{1-\varepsilon_1}{\varepsilon_1} + \frac{1}{F_{s-surr}} + \frac{1-\varepsilon_2}{\varepsilon_2}} \qquad 3.27$$

$F_{s-surr}$ is the view factor from a surface to the surroundings, given in equation 3.28, $\varepsilon_1$ is the emissivity of the outgoing radiating surface (the heat sink) and $\varepsilon_2$ is the emissivity of the incoming radiating surface (the environment or shielding material).

$$F_{s-surr} = \frac{F_{1-4} + 2\bar{H}(F_{2-4})}{1 + 2\bar{H}} + \frac{2F_{1-5} + 2\bar{H}(2F_{2-5})}{1 + 2\bar{H}} \qquad 3.28$$

Where $\bar{H}$ is the non-dimensionalised fin height given in equation 3.29 with $\bar{L}$ the non-dimensionalised fin length. The view factor is split into 4 components: the view factor from heat sink surface 1, shown in figure 3.4, to surface 4 ($F_{1-4}$) and surfaces 5 and 6 ($F_{1-5}$), and the view factor from surfaces 2 and 3 to surface 4 ($F_{2-4}$) and surfaces 5 and 6 ($F_{2-5}$), given in equations 3.30 to 3.33. Figure 3.4 shows a single channel of a heat sink, comprising a base plate (surface 1), two fins (surfaces 2 and 3) and imaginary boundaries (surface 4, 5 and 6).

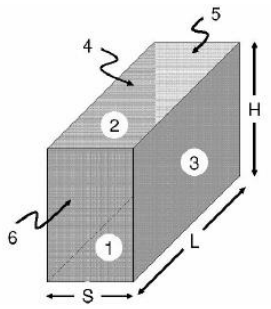


**Figure 3.4: A heat sink channel created by 2 fins and a base plate (Shabany, 2008)**

$$\bar{H} = \frac{H}{S}, \qquad \bar{L} = \frac{L}{S} \tag{3.29}$$

The view factors from each heat sink surface in figure 3.4 to the imaginary surfaces 4, 5 and 6 are given by the equations 3.30 to 3.33 (Shabany, 2010).

$$F_{1-4} = \frac{2\bar{H}^2}{\pi\bar{L}}\left\{\begin{array}{c} \ln\left(\frac{(\bar{H}^2+1)(\bar{H}^2+\bar{L}^2)}{(\bar{H}^2+\bar{L}^2+1)\bar{H}^2}\right)^{0.5} - \frac{1}{\bar{H}}\tan^{-1}\frac{1}{\bar{H}} - \frac{\bar{L}}{\bar{H}}\tan^{-1}\frac{\bar{L}}{\bar{H}} \\ + \frac{(\bar{H}^2+\bar{L}^2)^{0.5}}{\bar{H}^2}\tan^{-1}\frac{1}{(\bar{H}^2+\bar{L}^2)^{0.5}} + \frac{\bar{L}(\bar{H}^2+1)^{0.5}}{\bar{H}^2}\tan^{-1}\frac{\bar{L}}{(\bar{H}^2+1)^{0.5}} \end{array}\right\} \tag{3.30}$$

$$F_{1-5} = \frac{1}{\pi\bar{L}}\left\{\begin{array}{c} \bar{L}\tan^{-1}\left(\frac{1}{\bar{L}}\right) + \bar{H}\tan^{-1}\frac{1}{\bar{H}} - (\bar{L}^2+\bar{H}^2)^{0.5}\tan^{-1}\frac{1}{(\bar{L}^2+\bar{H}^2)^{0.5}} \\ + \frac{1}{4}\ln\left\{\left(\frac{(\bar{L}^2+1)(\bar{H}^2+1)}{\bar{H}^2+\bar{L}^2+1}\right)\left(\frac{(\bar{H}^2+\bar{L}^2+1)\bar{L}^2}{(\bar{L}^2+1)(\bar{H}^2+\bar{L}^2)}\right)^{\bar{L}^2}\left(\frac{\bar{H}^2(\bar{H}^2+\bar{L}^2+1)}{(\bar{H}^2+1)(\bar{H}^2+\bar{L}^2)}\right)^{\bar{H}^2}\right\} \end{array}\right\} \tag{3.31}$$

$$F_{2-4} = \frac{\bar{L}}{\pi\bar{H}}\left\{\begin{array}{c} \frac{1}{\bar{L}}\tan^{-1}\bar{L} + \frac{\bar{H}}{\bar{L}}\tan^{-1}\frac{\bar{L}}{\bar{H}} - \frac{(1+\bar{H}^2)^{0.5}}{\bar{L}}\tan^{-1}\frac{\bar{L}}{(1+\bar{H}^2)^{0.5}} \\ + \frac{1}{4}\ln\left\{\left(\frac{(\bar{L}^2+1)(\bar{H}^2+\bar{L}^2)}{(\bar{H}^2+\bar{L}^2+1)\bar{L}^2}\right)\left(\frac{(\bar{H}^2+\bar{L}^2+1)\bar{H}^2}{(\bar{H}^2+1)(\bar{H}^2+\bar{L}^2)}\right)^{\frac{\bar{H}^2}{\bar{L}^2}}\left(\frac{\bar{H}^2+\bar{L}^2+1}{(\bar{H}^2+1)(1+\bar{L}^2)}\right)^{\frac{1}{\bar{L}^2}}\right\} \end{array}\right\} \tag{3.32}$$

$$F_{2-5} = \frac{\bar{H}^2}{\pi\bar{L}}\left\{\begin{array}{c} \frac{1}{4}\ln\left\{\left(\frac{(\bar{H}^2+1)(\bar{H}^2+\bar{L}^2)}{(\bar{H}^2+\bar{L}^2+1)\bar{H}^2}\right)\left(\frac{(\bar{H}^2+\bar{L}^2+1)\bar{L}^2}{(\bar{L}^2+1)(\bar{H}^2+\bar{L}^2)}\right)^{\frac{\bar{L}^2}{\bar{H}^2}}\left(\frac{\bar{H}^2+\bar{L}^2+1}{(\bar{H}^2+1)(1+\bar{L}^2)}\right)^{\frac{1}{\bar{H}^2}}\right\} \\ + \frac{\bar{L}}{\bar{H}}\tan^{-1}\frac{\bar{H}}{\bar{L}} + \frac{1}{\bar{H}}\tan^{-1}\bar{H} - \frac{(1+\bar{L}^2)^{0.5}}{\bar{H}}\tan^{-1}\frac{\bar{H}}{(1+\bar{L}^2)^{0.5}} \end{array}\right\} \tag{3.33}$$

These equations are used to eliminate the radiative component of the experimental heat transfer for an unshielded heat sink presented in section 6.2.1. This subsection does not consider the radiative impact of a shielded heat sink; this is given in the next subsection.

### 3.2.2. Shielded Heat Sink

For a shielded heat sink or a secondary segregated structure, as shown in figure 3.5, the shield is an active component in radiation. Using equation 3.28, nearly 75 % of the outgoing radiation from each channel would reach the imaginary surface 4 in figure 3.4. The flat surfaces (side surfaces in figure 3.3 and imaginary surface 4 in figure 3.4), of the heat sinks would emit nearly 85 % of the outgoing radiation to the closest shield section. The heat sinks have a high thermal conductivity and can be assumed to be uniform in temperature, as the efficiency calculated in equation 3.21 is >95 %, while the shielding material has a relatively low conductivity. The following assumptions are used to approximate the radiation component for the side, top and channel surfaces of the primary heat sink to the shield:

1. The shielding material is split into uniform temperature sections, as shown in figure 3.5.
2. The side and channel surfaces of the primary heat sink emit only to the $T_{shield1}$ surface while the secondary heat sink's side and channel surfaces emit to $T_{shield2}$ surface.
3. The top surface of the primary heat sink in a segregated structure only emits to the bottom surface of the secondary heat sink (and vice versa).
4. All other surfaces of the heat sink in a shielded or segregated structure configuration emit to the surrounding environment.

To quantify radiative heat transfer, using the assumptions above, equations 3.34 to 3.37 are used:

$$Q_{top} = \frac{\sigma(HtN + BW)\left(T_{surf}^4 - T_{hs2}^4\right)}{\frac{1}{\varepsilon_{hs1}} + \frac{1}{\varepsilon_{hs2}} - 1} \quad 3.34$$

$$Q_{bot} = \sigma\varepsilon_{hs1}(HtN + BW)\left(T_{surf}^4 - T_{surr}^4\right) \quad 3.35$$

$$Q_{side} = \frac{\sigma(4H + 2B + tN)L\left(T_{surf}^4 - T_{shield1}^4\right)}{\frac{1}{\varepsilon_{hs1}} + \frac{1}{\varepsilon_{shield}} - 1} \quad 3.36$$

The heat dissipated by radiation from the top, bottom and side (the surfaces shown in figure 3.3) are approximated using the emissivity of the heat sink ($\varepsilon_{hs1}$), the secondary heat sink ($\varepsilon_{hs2}$) and the shield ($\varepsilon_{shield}$) along with the fin height, fin thickness, base thickness, heat sink width, length, number of fins, the surface, shield and surrounding temperatures.

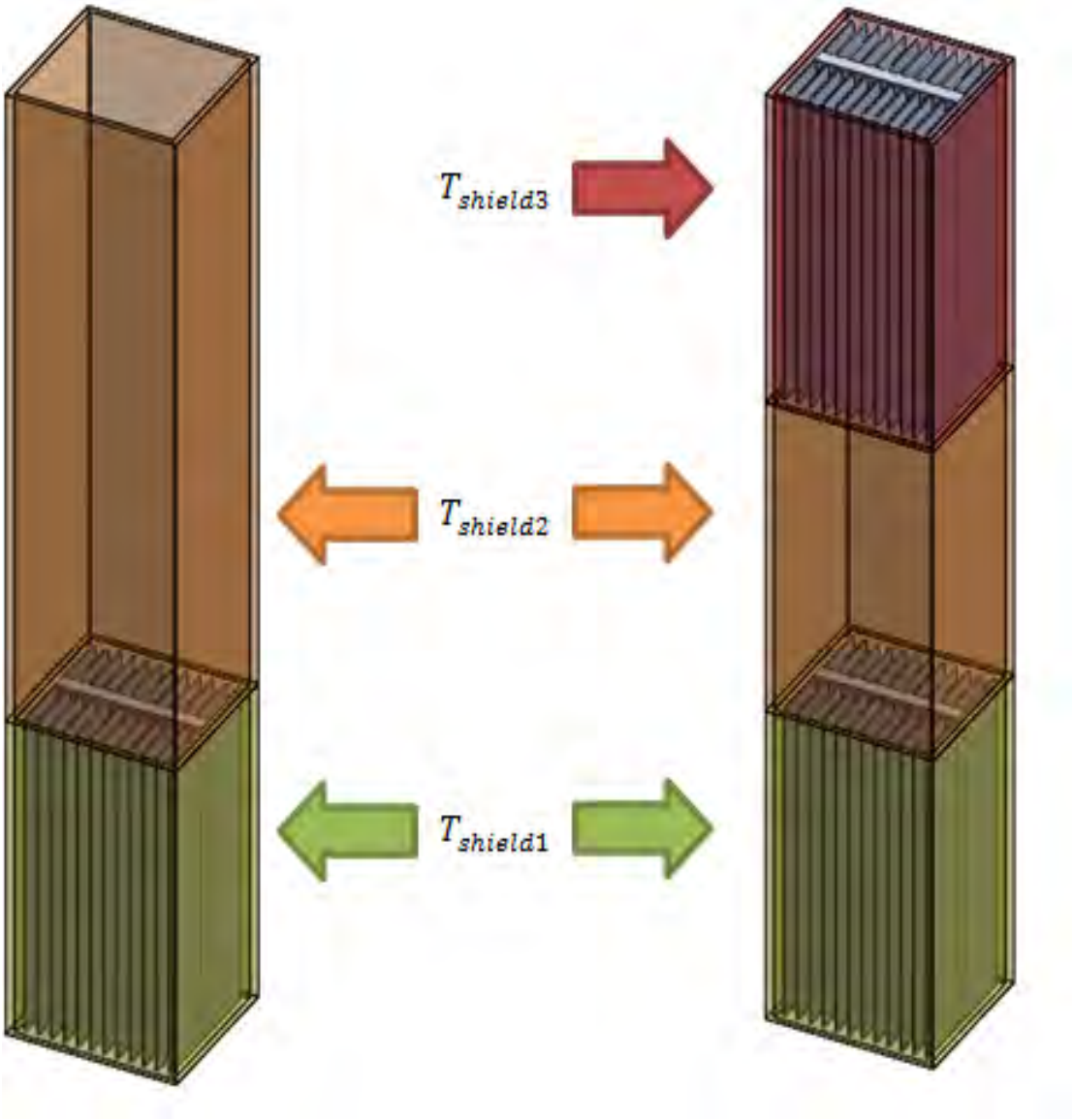


**Figure 3.5: Single shielded heat sinks (left) and secondary segregated structure (right)**

The radiative heat dissipation from a fin channel is given in the following equation:

$$Q_{channel} = \sigma(S + 2H)L\left(\hat{F}_4\left(T_{surf}^4 - T_{shield1}^4\right) + \hat{F}_5\left(T_{surf}^4 - T_{surr}^4\right)\right) \quad 3.37$$

The heat removed by radiation from each channel is calculated using the surface and the ambient temperatures, the fin height, fin spacing and the exact view factor for surfaces 4 ($\hat{F}_4$), 5 and 6 ($\hat{F}_5$) as shown in figure 3.4.

The exact view factor can be calculated using equation 3.38 (Shabany, 2008).

$$\hat{F}_4 = \frac{1}{\frac{1-\varepsilon}{\varepsilon} + \frac{1}{F_{4-surr}} + \frac{1-\varepsilon_2}{\varepsilon_2}} \qquad 3.38$$

$$\hat{F}_5 = \frac{1}{\frac{1-\varepsilon}{\varepsilon} + \frac{1}{F_{5-surr}} + \frac{1-\varepsilon_2}{\varepsilon_2}} \qquad 3.39$$

Where $\varepsilon_2$ is the emissivity of the shielding material, $F_{4-surr}$ and $F_{5-surr}$ are the view factors from surfaces 1, 2 and 3 to surface 4 and surface 5, shown in figure 3.4, and given in equations 3.40 and 3.41 respectively:

$$F_{4-surr} = \frac{F_{1-4} + 2\bar{H}(F_{2-4})}{1 + 2\bar{H}} \qquad 3.40$$

$$F_{5-surr} = \frac{2F_{1-5} + 2\bar{H}(2F_{2-5})}{1 + 2\bar{H}} \qquad 3.41$$

Where $\bar{H}$ is given in equation 3.29 and $F_{1-4}$, $F_{1-5}$, $F_{2-4}$ and $F_{2-5}$ are given in equations 3.30 to 3.33.

## 3.3. Conclusions

The equations for calculating the optimum spacing of an unshielded natural convection heat sink are presented. Methods to calculate the radiative and convective heat dissipation for an optimally designed natural convection heat sink are also presented. Assumptions are provided to calculate the radiative heat dissipation in a shielded or segregated structure. These methods are used to calculate radiative heat transfer radiation from the experimental testing facility and create an analytical model based on previous works. The next chapter will discuss the approach taken to compute the numerical model of the heat sink in an unshielded, shielded and a segregated structure.

# 4. Numerical Modelling

This chapter is split into three sections; the first section presents the governing equations for modelling flow and radiation using Star-CCM+ v6.02.007. The second section describes a mesh independence study on the geometry investigated. The last section, section 4.3, provides a summary of the information presented in this chapter.

## 4.1. Theory

This section details the governing equations and the radiation relations to calculate convective and radiative heat transfer, respectively, for the numerical calculations. The first subsection presents the Navier-Stokes equations for laminar natural convection, incorporating the Boussinesq approximation. The second subsection describes the technique that STAR-CCM+ uses to calculate radiation.

### 4.1.1. Governing Equations

Star-CCM+ solves the Navier-Stokes equations in continuous integral form using the SIMPLE algorithm (Cd-Adapco, 2010). The mass, energy and momentum equations are listed in integral form in equations 4.1, 4.2 and 4.3 respectively.

$$\frac{d}{dt}\int_V \rho\chi dV + \oint_A \rho(\mathbf{v}-\mathbf{v}_g)\cdot d\mathbf{a} = 0 \qquad 4.1$$

Where $\chi$ is the porosity, $\rho$ is the density, $V$ is the cell volume, $\mathbf{v}$ is the velocity vector, $\mathbf{v}_g$ is the grid velocity and $\mathbf{a}$ is the face area vector.

The energy transport equation in solid cells is:

$$\frac{d}{dt}\int_V \rho C_p T dV = -\oint_A \mathbf{q}''\cdot d\mathbf{a} \qquad 4.2$$

Where $\rho$ is the solid density, $C_p$ is the specific heat, $\mathbf{q}''$ is the heat flux vector and $T$ is the temperature.

The integral form of the momentum equations is given as follows:

$$\frac{d}{dt}\int_V \rho\chi\mathbf{v}dV + \oint_A \rho\mathbf{v}(\mathbf{v}-\mathbf{v}_g)\cdot d\mathbf{a} = -\oint_A \rho\mathbf{I}\cdot d\mathbf{a} + \oint_A \mathbf{T}\cdot d\mathbf{a} + \int_V \mathbf{f}dV \qquad 4.3$$

The terms on the left-hand side of the momentum equation are the transient term and the convective flux; on the right-hand side are the pressure gradient term, the viscous flux and the body force terms respectively. $\mathbf{T}$ is the viscous stress tensor given in equation

4.4, **I** is the identity matrix and **f** is given in equation 4.5 for buoyancy induced body forces evaluated with the Boussinesq approximation.

The stress tensor, **T**, in the case of natural convection heat sinks is laminar flow which is given by:

$$\mathbf{T} = \mathbf{T}_l = \mu\left[\nabla\mathbf{v} + \nabla\mathbf{v}^T - \frac{2}{3}(\nabla\cdot\mathbf{v})\mathbf{I}\right] \qquad 4.4$$

Where $\mathbf{T}_l$ is the stress tensor for laminar flow, $\mu$ is the dynamic viscosity and $T$ is the temperature.

The Boussinesq approximation is used to neglect density differences, except where they appear in terms multiplied by g, the acceleration due to gravity. This correlates the coefficient of volumetric expansion with the acceleration due to gravity as a product in the buoyancy induced body force. The buoyancy induced body force using the Boussinesq approximation is given as:

$$\mathbf{f} = \rho\mathbf{g}\beta(T - T_{ref}) \qquad 4.5$$

Where **g** is the gravitational vector, β is the thermal expansion coefficient and $T_{ref}$, the reference temperature. For the analysis in this thesis, the reference temperature is equal to the ambient temperature.

### 4.1.2. Surface-to-Surface Radiation

The net radiant flux from each surface is a function of the surface properties and the thermal boundary conditions imposed on that surface (Cd-Adapco, 2010). Surfaces are represented as a collection of polygons called patches; view factors are calculated for each pair of patches with the emissive power and radiation properties assumed to be uniform over the surface of each patch. For the geometry under investigation, the surface mesh acts as the patch.

View factors depends on the surface geometry, as the geometry is fixed; view factors are obtained once at the start of the simulation.

An example of a patch (surface $dS_1$ and $dS_2$) view factor can be seen in figure 4.1.

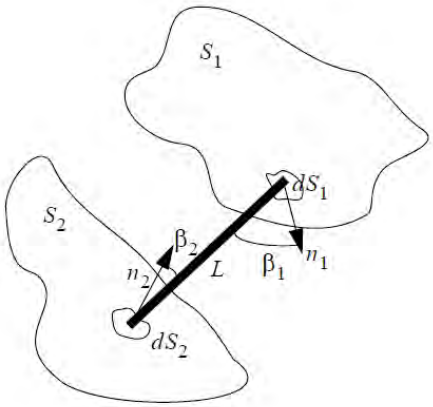


Figure 4.1: View factors between two finite surfaces (Cd-Adapco, 2010)

The total amount of radiation power emitted by surface $dS_1$ on surface $dS_2$ is given in equation 4.6 with the view factor given in equation 4.7:

$$P_{1-2} = \frac{\int_{S_1}\int_{S_2}(\pi i_1' \frac{\cos(\beta_1)\cos(\beta_2)}{\pi L^2} dS_1 dS_2}{i_1' S_1} \quad 4.6$$

$$F_{1-2} = \frac{1}{S_1}\int_{S_1}\int_{S_2} \frac{\cos(\beta_1)\cos(\beta_2)}{\pi L^2} dS_1 dS_2 \quad 4.7$$

Where $P_{1-2}$ is the total power leaving surface 1 and incident on surface 2, $S_1$ is the surface area, $i_1'$ is the total intensity leaving surface 1, $L$ is the distance and $\beta_1$ angle between the surface normal and a line joining surfaces 1 and 2.

The view factor for surface $dS_2$ on surface $dS_1$ is given in equation 4.8, alternatively it can be written as equation 4.9 usually called the reciprocity condition:

$$F_{2-1} = \frac{1}{S_2}\int_{S_2}\int_{S_1} \frac{\cos(\beta_1)\cos(\beta_2)}{\pi L^2} dS_1 dS_2 \quad 4.8$$

$$F_{2-1} = F_{1-2}\frac{S_1}{S_2} \quad 4.9$$

Where $F_{2-1}$ is the view factor for a pair of patches from surface 2 to surface 1 and $S_2$ is the surface area.

## 4.2. Mesh Details

This section is split into five subsections used to determine the optimum mesh parameters for the numerical simulation. A typical mesh of a heat sink and shield is shown in figure 4.2 with the mesh parameters investigated are the characteristic

dimension of the mesh (base size), number of layers generated at boundary surfaces (prism layers) and the overall thickness of these prism layers.

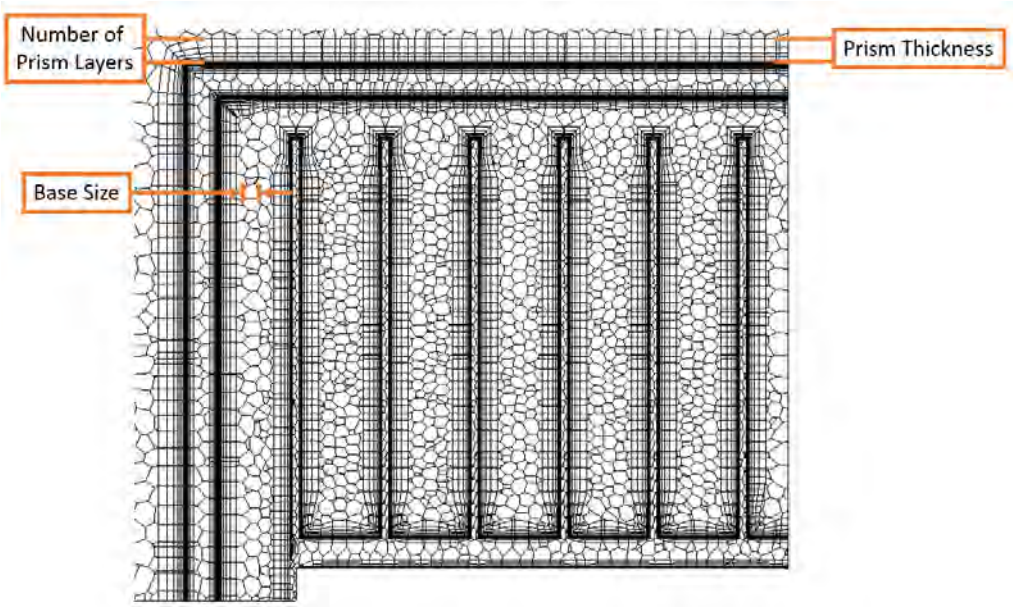


Figure 4.2: Numerical Mesh Properties

The first subsection describes the initial parameters used to establish the base test case. The next subsection varies the base size while keeping the other meshing parameters constant. The next subsection utilises the base size determined from the second subsection while changing the number of boundary layer meshes (called prism layers). The fourth subsection utilises the number of prism layers from the third subsection while changing the prism layer thickness. The last subsection compares the results to established literature. The parameters were considered independently meshed when the output varied by less than 1% for a change in the mesh properties.

### 4.2.1. Initial Parameters

To ensure that the simulations were independent of cell size, a mesh independence study was conducted for an unshielded heat sink, given in figure 2.3 in section 2.2, with a base plate temperature of 65 ℃ above ambient temperature, the largest temperature differential investigated in this thesis, as stated in section 2.2, and operating at an ambient temperature of 26.9 ℃, the default ambient temperature in Star-CCM+. The mesh was created using a polyhedral mesher, with prism layer mesh and the surface remesher in Star-CCM+ v6.02.007 on a 64-bit Windows 7 computer. The heat sink under investigation in this thesis is a double sided heat sink as shown in figure 2.3 in section 2.2. Due to the symmetry of this heat sink, only a quarter of it was modelled

with symmetry planes used, as shown in figure 4.3, to reduce computing time and resources as the model is symmetrical.

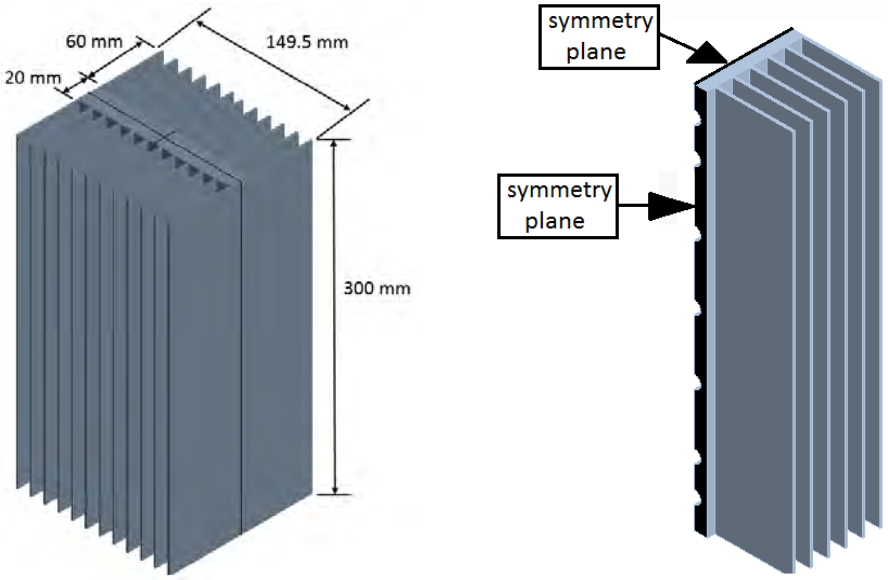


Figure 4.3: The geometry of the unshielded heat sink (left) and simulated heat sink (right)

The simulation monitored heat dissipation of the entire heat sink and the maximum velocity at the midsection of the primary heat sink, shown in figure 4.4 as the velocity monitor plane. These two points were chosen as heat dissipation is the quantity of interest from the heat sink, while the maximum velocity at the midsection was chosen to ensure that the fluid flow was consistent in the channels. The solution criteria required the maximum velocity to have a standard deviation of less than 0.003 $ms^{-1}$ and the heat dissipation to be less than 0.05 W (this equates to <0.1 % of the analytical solution when calculated using equation 3.8 in section 3.1) over 50 iterations.

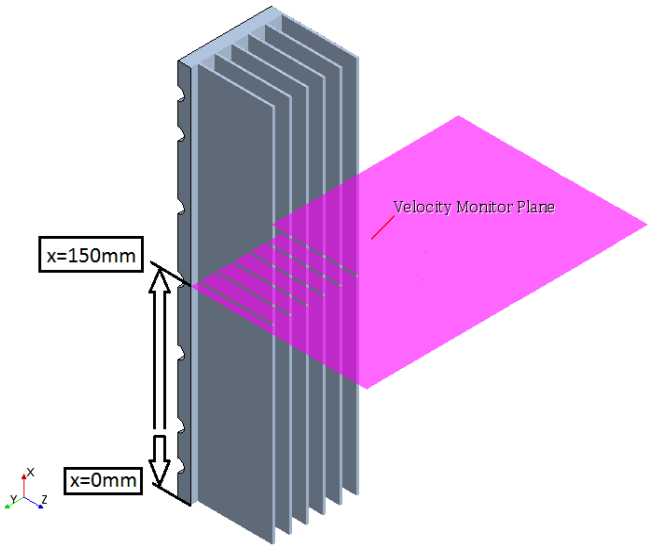


Figure 4.4: Location of the maximum velocity plane

### 4.2.2. Base Size

In order to ensure that the mesh was independent of base size, the mesh parameters were maintained constant with 8 prism layers at a prism thickness of 4 mm. The base size of the mesh was varied; starting at 10 mm and decreased in steps of 1 mm until the heat dissipation and velocity changed by less than 1 %. Figure 4.5 shows the heat dissipation and maximum velocity plotted against the base size. As the base size decreased, the number of cells in the mesh increased and the heat dissipation and maximum velocity changed. The heat dissipation and maximum velocity start to level off at a base size of 6mm; at this point, the velocity and heat dissipation were found to change by less than 1 %, ensuring mesh independency.

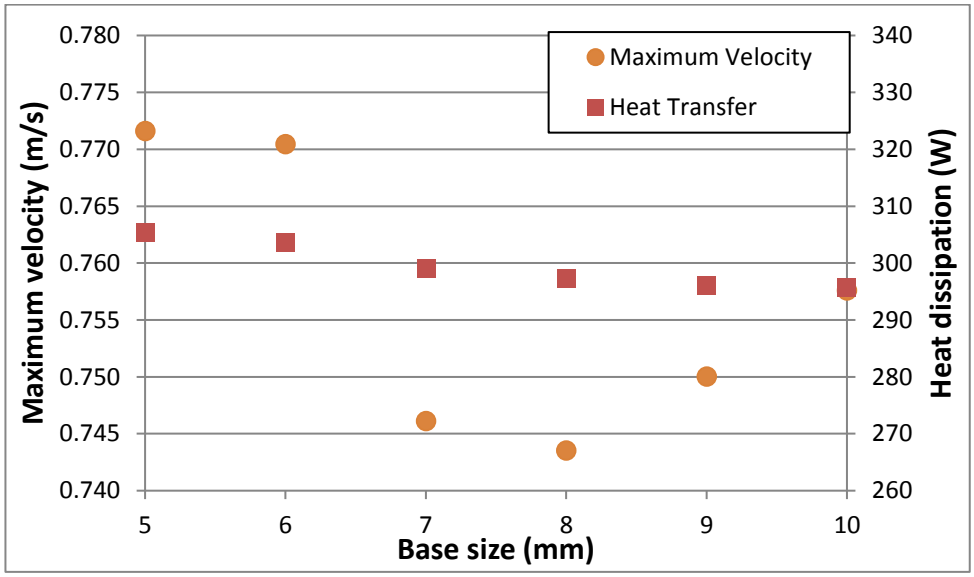


**Figure 4.5: Heat dissipation and maximum velocity plotted as a function of cell base size at 8 prism layers and a prism thickness of 4mm.**

### 4.2.3. Number of Prism Layers

The base cell size and prism layer thickness were held constant at 6mm and 4mm thick, respectively. The number of prism layers was changed from 2 to 10 layers in steps of 2. Figure 4.6 shows the heat dissipation and maximum velocity plotted against the number of prism layers. As the number of prism layers increased, the number of cells in the boundary layer increased and the heat dissipation and maximum velocity were found to vary by less than 1% at 4 prism layers up to 10 prism layers. A comparison of the prism layer to experimental values, shown in section 4.2.5, determined that the optimum number of prism layers was 10 layers.

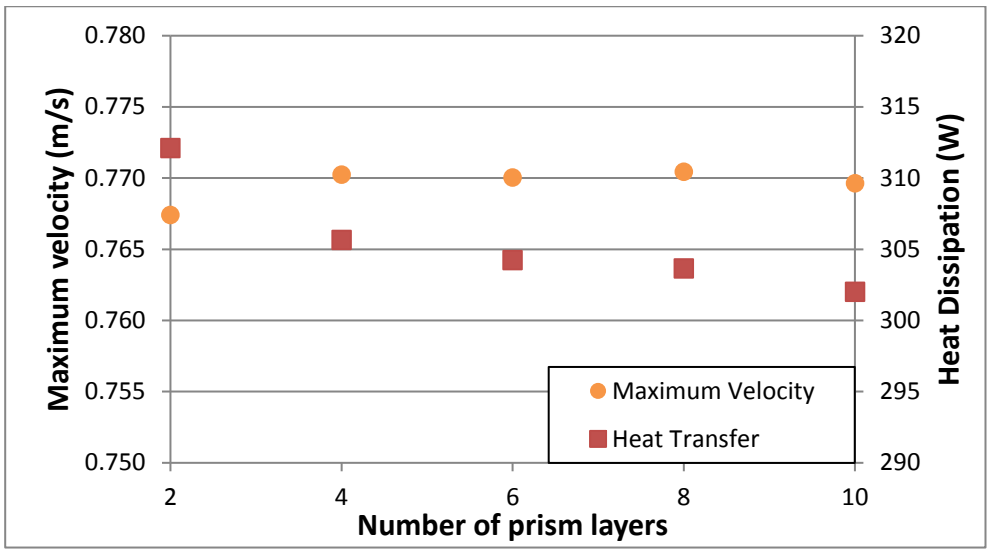


Figure 4.6: Heat dissipation and maximum velocity plotted as a function of the number of prism layers at 8mm base size and a prism thickness of 4mm.

### 4.2.4. Prism Layer Thickness

The thickness of the prism layer was varied while the base size and the number of prism layers were set at 6mm and 10 layers respectively, as determined in the previous subsections. The prism layer thickness was varied; starting at 3.5 mm and increased in steps of 0.5 mm until the heat dissipation and velocity changed by less than 1 %. Figure 4.7 shows the heat dissipation and maximum velocity plotted against the prism layer thickness. The heat dissipation and maximum velocity start to level off at a prism layer thickness of 5 mm; at this point, the velocity and heat dissipation were noted to change by less than 0.5 %.

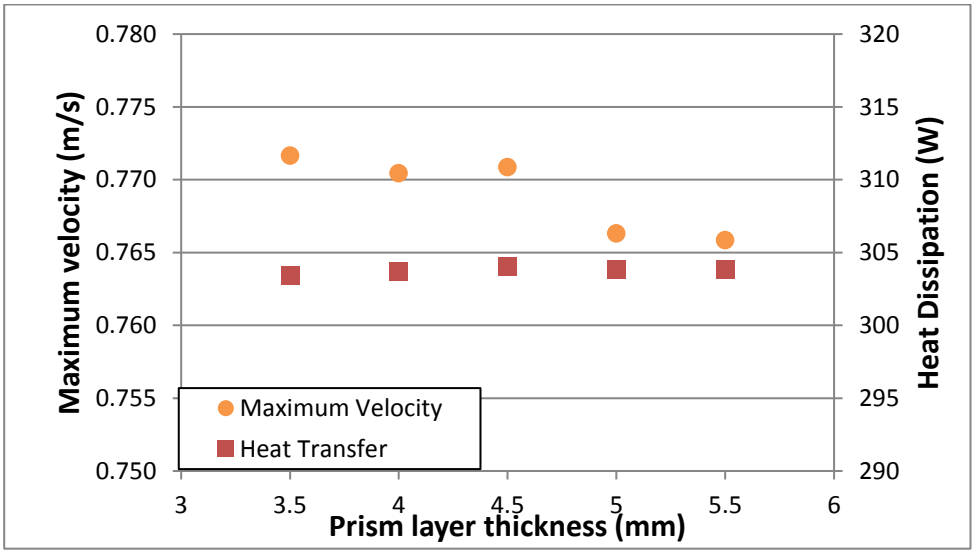


Figure 4.7: Heat dissipation and maximum velocity plotted against prism layer thickness at 10 prism layers and 8mm base size.

### 4.2.5. Mesh Validation

In this subsection, numerical results from the independent mesh of 6 mm base thickness with 10 prism layers at a prism thickness of 5 mm, obtained from the previous subsections, are compared to experimental results found in literature (Oosthuizen, 1984). While the heat dissipation is in line with theory calculated in equation 3.8 in section 3.1, the boundary layer must be checked to ensure it is being modelled appropriately. The boundary layer profile was taken at X=150 mm, as shown in figure 4.3, as the velocity monitor plane, and compared to experimental results presented by Ostrach (1953) and Oosthuizen (1984). Both authors used dimensionless temperature function (equation 4.10) and dimensionless distance (equation 4.11) which are given in equations 4.10 and 4.11 respectively:

$$H(\eta) = \frac{T - T_\infty}{T_{surf} - T_\infty} \qquad 4.10$$

Where $H(\eta)$ is the dimensionless temperature function, $T$ is the temperature at a point, $T_\infty$ is the ambient air temperature and $T_{surf}$ is the surface temperature.

$$\eta = \left(\frac{Gr_x}{4}\right)^{\frac{1}{4}} \left(\frac{Y}{X}\right) \qquad 4.11$$

Where $\eta$ is a dimensionless similarity variable, $Gr_x$ is the Grashof number, $Y$ and $X$ are the Cartesian coordinates from the leading edge, in this case the base plate of the heat sink.

The dimensionless temperature boundary layer is plotted against dimensionless distance in figure 4.8. The mesh, with a 5mm thick prism layer, provided an average deviation of 1.6 % from the theoretical boundary line given by Ostrich (1953), experimentally verified by Oosthuizen (1984), deemed to be an acceptable discrepancy for this thesis.

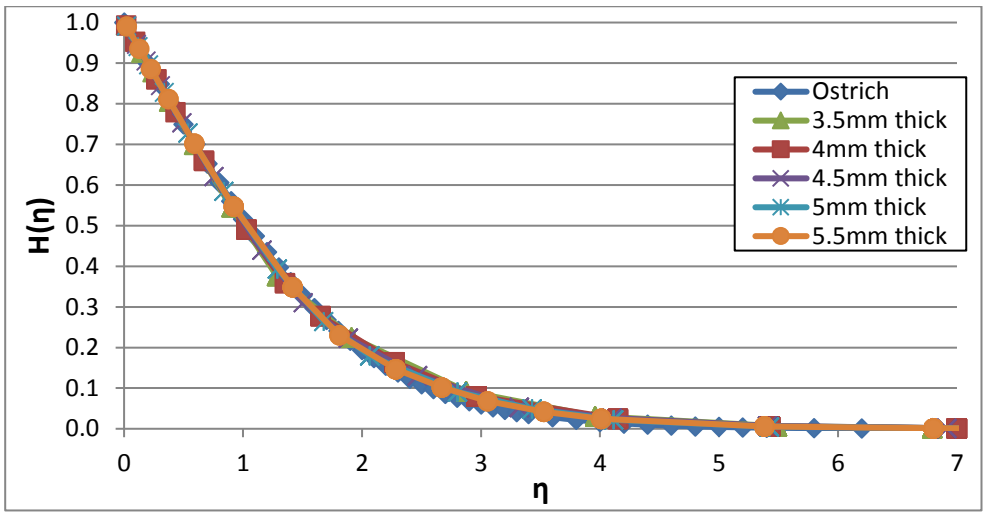


**Figure 4.8: Dimensionless temperature for various prism layer thicknesses as a function of dimensionless distance at X=150mm**

## 4.3. Summary

This chapter presented the governing equations used by Star-CCM+ v6.02.007 to model radiation and natural convection laminar flow used in this thesis. A mesh independence study was carried out on the geometry investigated, and found a base size of 8 mm, 10 prism layers and prism thickness of 5 mm to be independent. This mesh provided an average deviation of 1.6 % from the theoretical boundary line given by Ostrich (1953) and from experimental data by Oosthuizen (1984); this was deemed to be an acceptable discrepancy for this thesis. The next chapter will discuss the experimental apparatus and procedure to experimentally model the heat sink in an unshielded, shielded and a segregated structure.

# 5. Experimentation

This section is split into seven sections; the first section describes the preparation of the heat sink and shielding material. The second section describes how power in the cartridge heaters was quantified, and the third section defines how the radiation properties were determined. The fourth section describes how the experimental values were obtained to calculate the Nusselt and Elenbaas numbers. The fifth section describes the procedure involved to experimentally test unshielded, shielded and segregated structures, and the sixth section examines the uncertainties associated with all experimental parameters in this study. The seventh section provides a list of all experimentally obtained values and a list of experimentally derived values.

## 5.1. Apparatus

This section describes the dimensions and properties of the heat sink and the shield used in the experimental setup. The first section describes the properties and the process to manufacture the heat sink. The second subsection describes the features of the shielding material and, finally, the environmental shielding.

### 5.1.1. Heat Sink Preparation

Two aluminium 6082T6 blocks, with dimensions of 0.15 m x 0.15 m x 0.31 m, were machined, in an Optimum BF46 Vario milling machine with a tolerance of ±0.25 mm, to a heat sink representative of a typical RRH, shown in figure 2.3 and detailed in section 2.2, and whose dimensions are listed in table 5.1. The heat sinks were double sided (fins both sides of the base plate) in order to negate uncertainties due to losses from the baseplate of a single sided structure, and they were anodized black in order to accurately quantify radiative losses.

Table 5.1: Geometric properties of the heat sink

| Symbol | Dimensions | Symbol | Dimensions |
|---|---|---|---|
| $W$ | 149.5 mm | $t$ | 1.9 mm |
| $L$ | 300.0 mm | $B$ | 20.0 mm |
| $H$ | 60.0 mm | $S$ | 11.5 mm |
| N | 24 | | |

Seven 10 mm diameter and 150 mm long cartridge heaters, coated in Dow Corning 2265931 heat sink compound with a thermal conductivity of 0.67 $Wm^{-1}$ $K^{-1}$, were embedded into the base plate of each heat sink, shown on the left of figure 5.1. Ten 1

mm diameter thermocouple holes were drilled at specific depths and locations, shown on the right of figure 5.1.

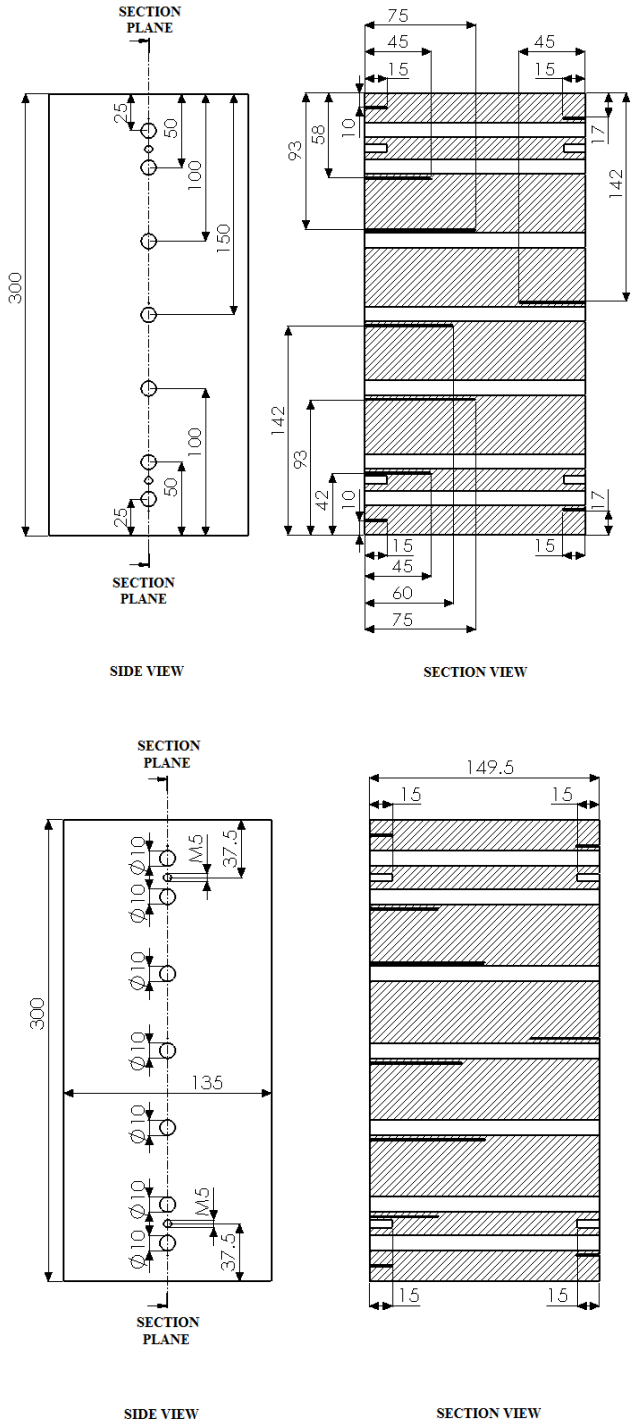


**Figure 5.1: Heat sink with locations for cartridge heaters (left) and thermocouple holes inside the base plate of the heat sink (right)**

Four M5 screw holes were drilled into the heat sink to facilitate four nylon screws to suspend the heat sink, shown in figure 5.1. The low conductivity of the Nylon screws, ~0.25 $Wm^{-1}K^{-1}$, minimised the amount of conductive heat loss transferred through the screws.

### 5.1.2. Shield Preparation

The shielding material was made from polycarbonate with a nominal thermal conductivity of ~0.19 $Wm^{-1}K^{-1}$. The shield did not cover the top and bottom of the heat sink, in order to allow air to flow freely. The shielding was connected using nylon screws with adjoining sides sealed in tape to reduce the possibility of airflow from the gap between two adjacent polycarbonate pieces.

The heat sink shield featured 6mm and 8mm thick polycarbonate with a length of 900 mm, as shown in figure 5.2. M5 screw holes facilitated a clearance of 5.75 mm from the shield and the heat sink. Metal profiling supported the shield 300 mm off the ground allowing the shield to be adjusted to ensure that it was level.

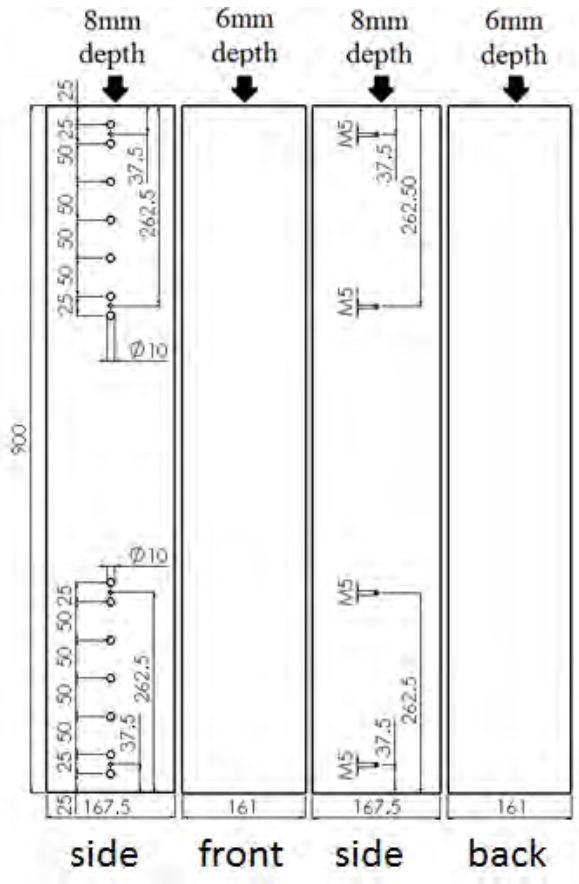


Figure 5.2: Polycarbonate shielding material

A polycarbonate environmental shield protected the testing area reducing the effects of air currents in the laboratory. This structure was over five times the length of the heat sink at 1550 mm and over three times the width and height at 550 mm and 460 mm respectively. The environmental shield was propped up, 50 mm off the ground, to allow air into the testing section as shown in figure 5.3.

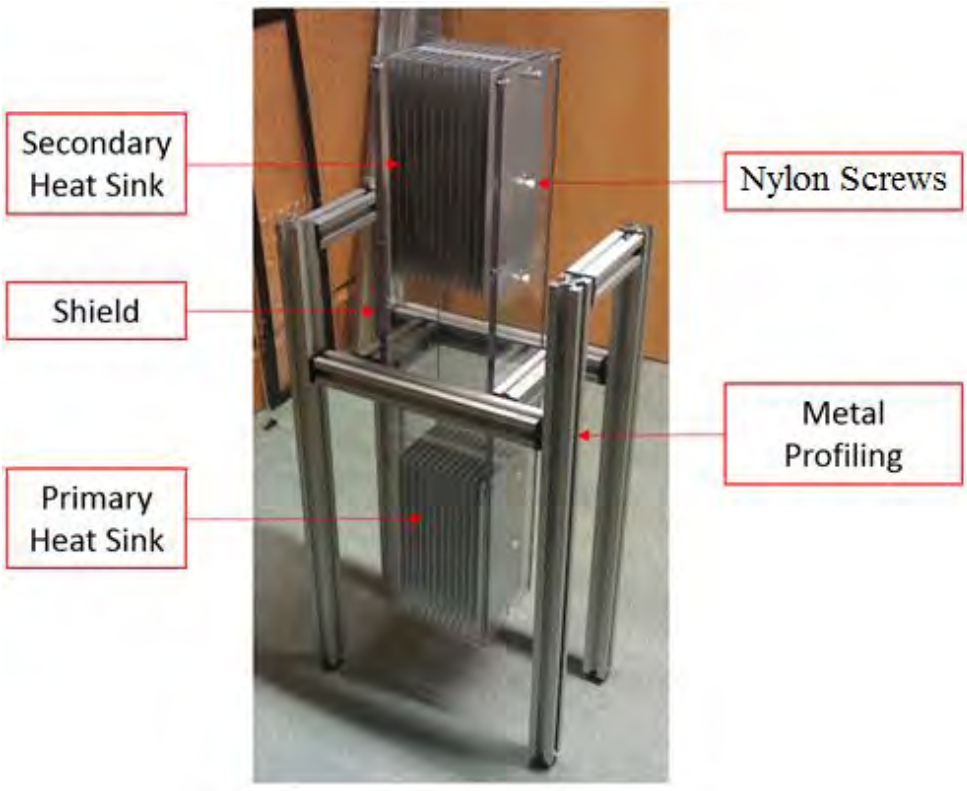


Figure 5.3: Experimental setup of a segregated heat sink structure

## 5.2. Power

This section describes how the power dissipated in the cartridge heaters was measured. The first subsection gives details of the devices used to supply and measure power in the test facility. The next subsection discusses the relations applied to experimental values to obtain the power measurement, and finally, the last subsection details the procedure for obtaining these experimental values.

### 5.2.1. Facility

BSI PSM 3/2A, Sorensen DCS 80-37 and Delta Elektronika SM 3004-D power supplies were used to provide a constant voltage to each cartridge heater. LabVIEW 2011 and the LabVIEW 2011 PID modules provided PID control to each individual heater, using feedback from seven Labfacility Z2-K-2M (IEC) K-type thermocouples, shown in figure 5.1, to vary the duty cycle of a pulse-width modulated (PWM) digital output. A National Instruments PCI-6229 card and a CB-68LP connector block generated the PWM digital output which switched a Crydom D2D07 relay turning on or off the power to the cartridge heaters. A circuit diagram showing a single path for heaters, resistors and relays in parallel as shown in figure 5.4.

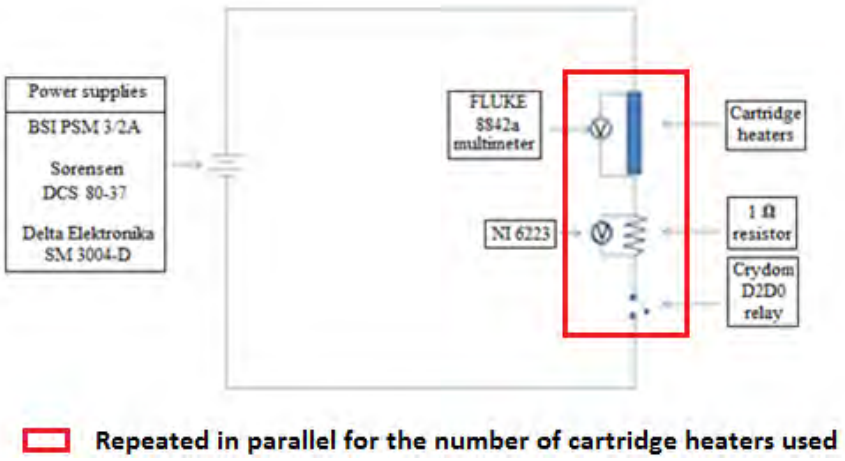


Figure 5.4: Circuit diagram of a single path for the resistors, cartridge heaters and relays used in the experimental setup

In order to accurately measure the voltage drop in the heating element, the cartridge heater wire was exposed as close as possible to the heating element and an additional wire was soldered to this exposed wire. For safety, the exposed wire and soldered wire were covered in shrink wrap plastic; this process, a 4-wire configuration, is shown in figure 5.5.

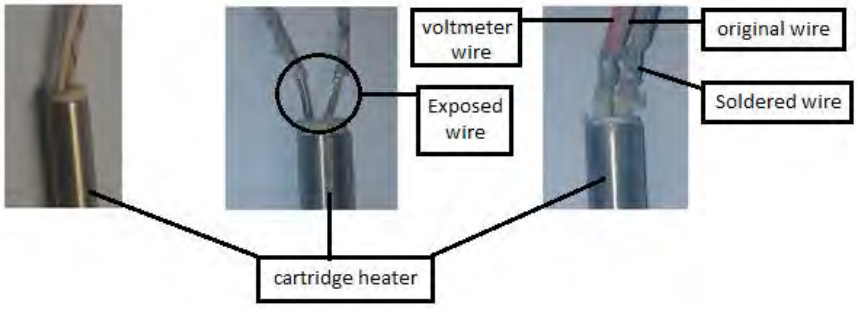


Figure 5.5: Unexposed wire (left), exposed wire (centre) and soldered wire (right)

### 5.2.2. Calculation of Power

Total power in each heat sink ($P$) is calculated, using equation 5.1, as the time average of the sum of each individual voltage drop in the cartridge heaters times the current flowing through the resistor connected in series to each individual cartridge heater:

$$P = \frac{1}{\mathrm{t}} \int_0^t \sum V_h I_R \qquad 5.1$$

The voltage drop across a cartridge heater ($V_h$) was measured using a calibrated FLUKE 8842a multimeter (calibration cert is presented in Appendix B), connected as close as possible to the cartridge heater. A National Instruments PCI-6229 card with a CB-68LP connector block, calibrated from the FLUKE 8842a, was used to record the voltage drop

in each individual resistor ($V_R$), of known resistance ($R$), connected in series to each heater to calculate the current, given in equation 5.2:

$$I_R = \frac{V_R}{R} \qquad 5.2$$

## 5.3. Radiation Properties

In this section, the emissivity of the heat sinks are obtained using the process outlined in Kim *et al.* (2013). To calculate radiative losses, a Labfacility Z2-K-2M (IEC) K-type thermocouple probe was attached to the heat sink at different locations and monitored at different temperatures using a FLUKE Ti32 handheld thermal imager. The emissivity of the heat sink was calculated using equation 5.3:

$$\varepsilon = \frac{T_{IR}^4 - T_{amb}^4}{T_{surf}^4 - T_{amb}^4} \qquad 5.3$$

In equation 5.3, $\varepsilon$ is the emissivity of the object, $T_{IR}$ is the temperature measured by the IR camera, $T_{surf}$ and $T_{amb}$ are the surface and ambient temperatures, respectively. These were measured using a calibrated thermocouple probe. The heat sink was found to have an average emissivity of 0.97, as calculated using equation 5.3, with a sample IR image shown in figure 5.6. The polycarbonate was also measured to have an emissivity of 0.95.

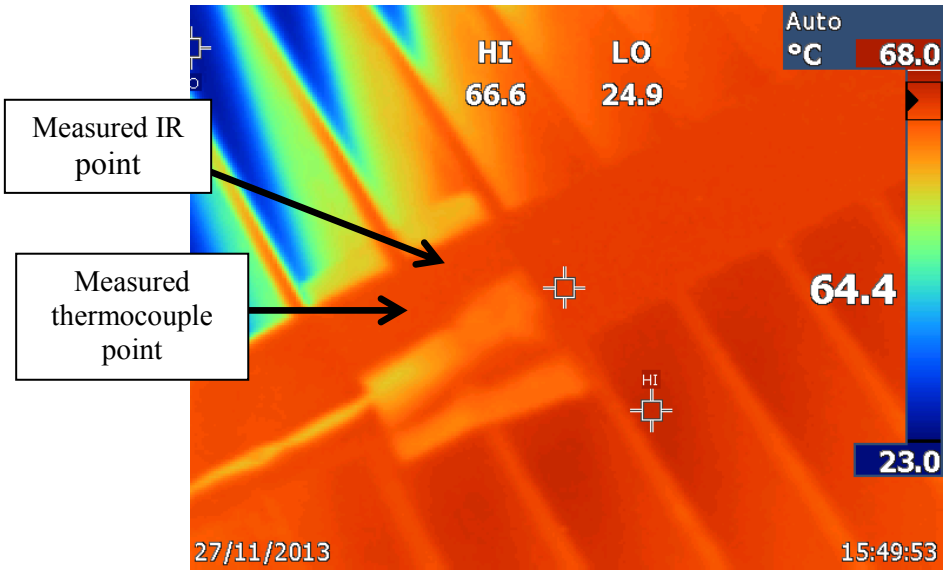


Figure 5.6: Thermal camera image of the top surface of the heat sink

## 5.4. Non-Dimensional Numbers

This section is split into two subsections describing how the non-dimensional numbers, Nusselt and Rayleigh, were calculated. The first subsection gives details of how

temperature was measured in the test facility. The next subsection discusses the relations applied to reduce the data obtained.

### 5.4.1. Facility

Temperature was monitored using K-type thermocouples, recorded using a Red Lion T1611100 controller, five Eurotherm 2132i controllers, a National Instruments TBX-68T and a National Instruments USB-TC01, shown in figure 5.7. The thermocouples were calibrated to ±0.1 ℃ using a Lauda E100 water bath and a calibrated FLUKE 1504 digital thermometer (calibration certificate is shown in Appendix C) as a temperature reference.

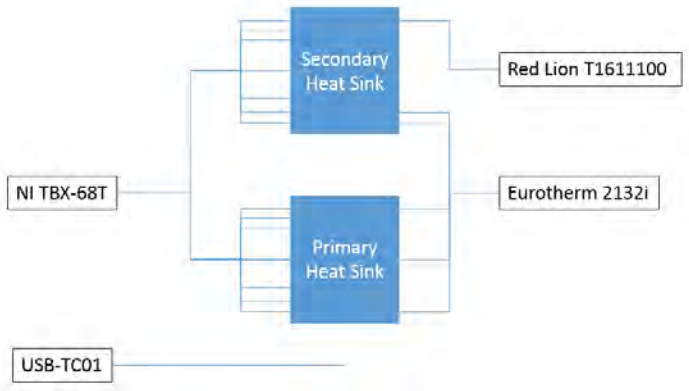


**Figure 5.7: A schematic of the Eurotherm 2132i controllers, Red Lion T1611100, National Instruments TBX-68T and USB-TC01 thermocouple paths**

Ten thermocouples were located at different locations and depths inside the base of each heat sink as shown in figure 5.1 in section 5.1.1. Additional thermocouples were used to monitor the air temperature, the plume temperature and the chimney exit temperature as shown in figure 5.8. The thermocouples, exposed to air, were shrouded in aluminium foil with a thickness of 0.016 mm, which contained small punctures to allow air flow, a standard procedure in literature to eliminate radiation effects (Fisher & Torrance, 1999). These thermocouples were placed at the centreline of heat sink at the heights shown in figure 5.8.

The average temperature, recorded by the ten thermocouples in the base plate of the heat sink, was used to calculate values for radiation, the average Nusselt number, the average Elenbaas number and the film temperature.

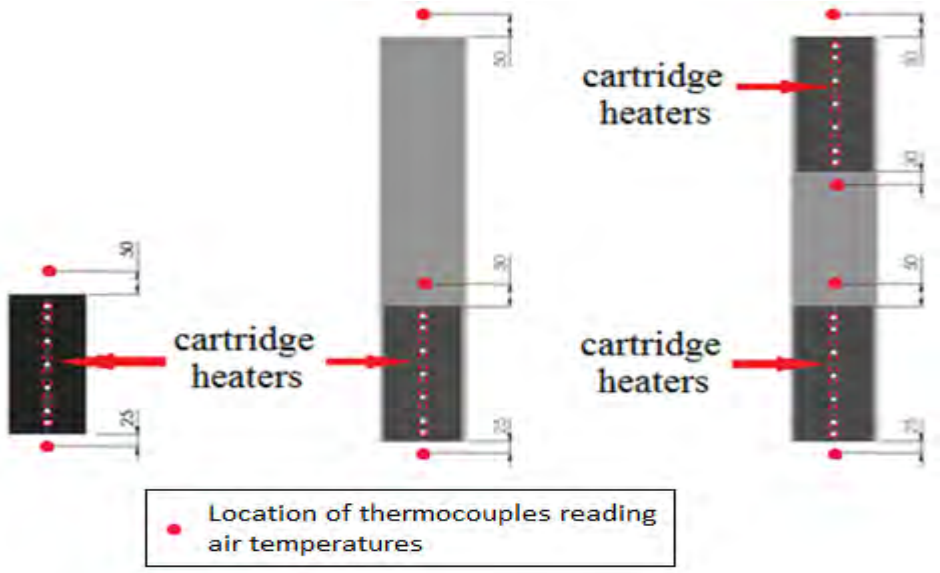


**Figure 5.8: Location of the thermocouple exposed to air in an unshielded (left), shielded (centre) and segregated structure (right)**

### 5.4.2. Data Reduction

To quantify the average Nusselt number and Elenbaas number, the radiative heat dissipation and the total power dissipated was calculated. Equation 5.4 gives the total heat dissipated by convection as the total heat dissipated minus the radiative heat dissipation:

$$Q_{conv} = P - Q_{rad} \qquad 5.4$$

$P$ is the total power dissipated in the heat sink calculated using equation 5.1 in section 5.2.2. $Q_{conv}$ is the heat dissipated via convection while $Q_{rad}$ is the heat dissipated by radiation, given in section 3.2.

After isolating the convective heat dissipation, the Nusselt number was calculated using equation 5.5.

$$\overline{Nu_s} = \frac{Q_{conv}S}{A_{hs}(T_{surf} - T_{amb})k_f} \qquad 5.5$$

The average Nusselt number ($\overline{Nu_s}$) over the entire surface of the heat sink was calculated using the total heat removed by convection, the entire heat sink area ($A_{hs}$) at a set base plate temperature ($T_{surf}$) above ambient temperature ($T_{amb}$) and the thermal conductivity of air ($k_f$). The properties of air are calculated at the film temperature ($T_{film}$), equation 5.6, by interpolating values from Appendix D.

$$T_{film} = \frac{T_{surf} + T_{amb}}{2} \qquad 5.6$$

## 5.5. Experimental Testing

This section is split into two subsections, the first subsection describes the experimental facilities used to test different heat sink configurations while the second subsection details the procedure undertaken to obtain experimental results.

### 5.5.1. Configuration

Three different configurations were tested; a single heat sink with no shield (unshielded), a single heat sink within an enclosure (shielded), and two heat sinks in a shield (segregated structure). The heat sinks are defined in section 5.1.1 and the shield is defined in section 5.1.2. An unshielded heat sink and a shielded heat sink can be seen in figure 5.9, while a secondary segregated structure can be seen in figure 5.10.

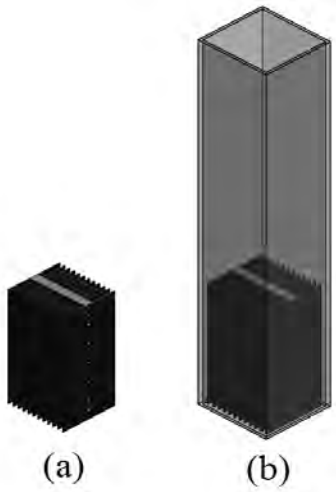


Figure 5.9: Unshielded heat sink (a) and shielded heat sink (b)

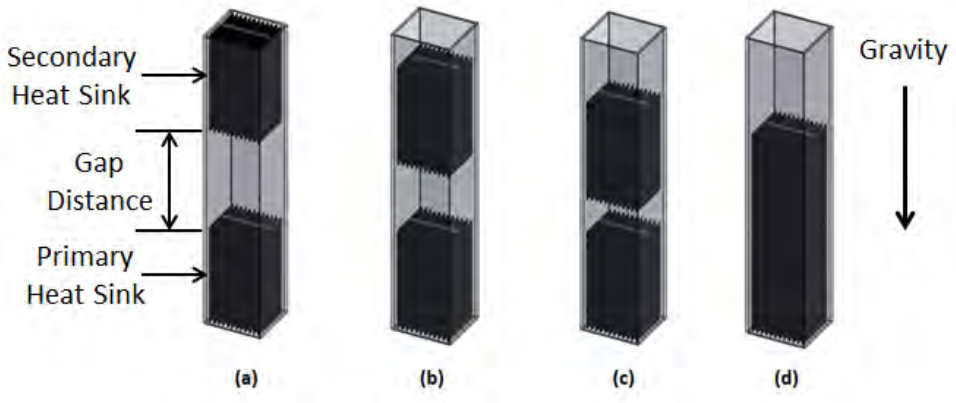


Figure 5.10: Segregated heat sink structures with varied heat sink gap; (a) 300mm (b) 200mm, (c) 100mm and (d) 5mm

### 5.5.2. Procedure

1. The unshielded heat sink was assembled using a bubble level to ensure the heat sink was flat.

2. The cartridge heaters were covered in thermal paste and inserted into the heat sinks; any excess thermal paste was removed. The air thermocouple was set up as shown in figure 5.8 in section 5.4.1.

3. The power supplies were turned on and the temperature set for the heat sink to a 5 degrees rise above ambient temperature. The voltage drop across each individual cartridge heater was recorded using the FLUKE 8842a multimeter.

4. The Crydom relays' on/off states changed based on temperature feedback, using LabVIEW 2011 and the National Instruments PCI-6229's digital output. The test facility was allowed to reach thermal equilibrium, usually up to one hour depending on the power supplied.

5. At thermal equilibrium, the voltage drop was recorded in each individual heater over a 10 minute period.

6. Steps 3 to 5 were repeated three times to minimize the effects of random fluctuations in the temperature and ambient environment, an established approach used in literature (Fisher & Torrance, 1999). The voltages were averaged over the three 10 minute periods.

7. Steps 3 to 6 were repeated for a 10, 15, 20, 25, 35, 45, 55 and 65 °C rise above ambient temperature.

8. The cartridge heaters were removed from the heat sink and the heat sink was positioned in the shield, as shown in figure 5.9, using nylon screws to ensure they are equidistant from the sides of the shielding material.

9. The cartridge heaters were covered in thermal paste and inserted into the heat sink through the holes in the shielding material; remove excess thermal paste was removed. This reduced the wire's interaction with the air flow; seal all gaps in the shield using sticky tape.

10. Steps 3 to 9 were repeated for a single heat sink in a shielded structure.

11. The secondary heat sink was inserted into the shielded structure at a gap distance of 300 mm. Steps 3 to 9 were repeated with an unheated secondary heat sink and a primary heat sink at temperatures of 25, 35, 45, 55 and 65 °C above ambient temperature.

12. The primary heat sink was set at 65 degrees above ambient and the secondary heat sink was set to 25 degrees above ambient temperature. Steps 3 to 9 were repeated for a primary heat sink at 65 °C above ambient and a secondary heat sink with temperatures of 25, 35, 45, 55 and 65 °C above ambient temperature.

13. The secondary heat sink was moved to a gap distance of 200 mm, 100 mm and 5 mm as shown as (b), (c) and (d) in figure 5.10. Steps 3 to 9 were repeated with an unheated secondary heat sink and a primary heat sink at temperatures of 25, 35, 45, 55 and 65 °C above ambient temperature.

## 5.6. Uncertainty Analysis

Experimentally measured values of temperature and voltage were used to calculate the thermophysical properties of air and the power dissipated in the heat sinks respectively. The uncertainty was calculated using the technique as outlined in equation 5.7 (Kline & McClintock, 1953).

$$w_R = \left[\left(\frac{\partial R}{\partial x_1} w_1\right)^2 + \left(\frac{\partial R}{\partial x_2} w_2\right)^2 + \cdots + \left(\frac{\partial R}{\partial x_n} w_n\right)^2\right]^{\frac{1}{2}} \qquad 5.7$$

Where $w_R$ is the resultant uncertainty, $w_1, w_2, .., w_n$ is the uncertainty in the independent variables and $\frac{\partial R}{\partial x_n}$ is the equation of interest differentiated by an independent variable.

The following values were recorded prior or during testing and their uncertainties were minimised:

- Length
- Temperature
- Air properties
- Radiation
- Power dissipated

This section has been divided into four subsections; the first three subsections detail the measurement uncertainty associated with the air properties, radiation and power

dissipated respectively. The last subsection presents the maximum uncertainty for each experimentally measured quantity.

### 5.6.1. Length

The heat sink was machined in an Optimum BF46 Vario with an accuracy of 0.25 mm; this provided an uncertainty of $\pm$0.5 mm when machining both sides. The dimensions of the heat sink were verified independently using Vernier Calipers. The dimensions of the shielding material also had an accuracy of $\pm$0.5 mm, independently verified using a steel ruler.

### 5.6.2. Temperature

Thermocouples were calibrated from a Lauda E100 waterbath and a calibrated FLUKE 1504 digital thermistor. The thermocouples were accurate to $\pm$0.1 K.

### 5.6.3. Air Properties

To minimise the uncertainty for the air properties, air values were taken at the film temperature, with an uncertainty of ±0.1 K, and interpolated from Table D.1 from section 5.4.2. The maximum uncertainty for the thermal conductivity, kinematic viscosity, density and Prandtl number was 0.3 %, 0.5 %, 0.1 % and 0.8 % respectively.

### 5.6.4. Radiation

Radiative properties were determined using the method shown in section 5.3 and calculated using equation 5.3. The emissivity was found to be 0.97 for the heat sink and 0.95 for the polycarbonate with a maximum uncertainty of ±0.02 using equation 5.3 from Kim *et al.* (2013). The view factor was calculated in section 3.2 using equation 3.27 and, using the method from Kline and McClintock in equation 5.7, produced a maximum uncertainty of 1.5%.

### 5.6.5. Power Dissipated

To minimise the uncertainty for the power dissipated, a FLUKE 8842a multimeter was calibrated to the manufacturer's specifications given in Appendix C, and used to measure the voltage drop in the cartridge heaters. A National Instruments PCI-6229, with a CB-68LP attachment, measured the current through each heat sink and was calibrated using the FLUKE 8842a to be within its specifications, calibrated using the following procedure:

1. A constant voltage was supplied to a 1 Ω resistor.
2. Readings from the FLUKE 8842a were recorded every 30 seconds over a 3 minute period, while the voltages in the PCI-6229 were recorded once every one twentieth of a second.
3. These readings, on the FLUKE 8842a and PCI-6229, were averaged over a 3 minute period.
4. Steps 1 to 3 were repeated from 0 to 3.6 V in steps of 0.1 V, to provide a calibration equation to convert readings from the PCI-6229 to the calibrated voltage from the FLUKE 8842a.
5. Steps 1 – 4 were repeated measuring the current using the FLUKE 8842a and comparing it with the calibration equation obtained in step 4.

Power was calculated using equation 5.1 from section 5.2.2 with a maximum percentage uncertainty of 0.07 %.

**Table 5.2: Uncertainty of experimentally calculated quantities**

| Parameter | Maximum uncertainty | Equation |
|---|---|---|
| $P$ | ±0.07 % | $\sum_{x=1}^{7} V_{h_x} \frac{V_{R_x}}{R}$ |
| $Q_{rad}$ | ±7.1 % | $\eta_r\left(Q_{top} + Q_{bot} + Q_{side} + (\mathrm{N}-2)Q_{channel}\right)$ |
| $Q_{top}$ | ±5.18 % | $\sigma\varepsilon(HtN + BW)\left(T_{surf}^4 - T_{surr}^4\right)$ |
| $Q_{bot}$ | ±5.18 % | $\sigma\varepsilon(HtN + BW)\left(T_{surf}^4 - T_{surr}^4\right)$ |
| $Q_{side}$ | ±5.2 % | $\sigma\varepsilon(4H + 2B + tN)L\left(T_{surf}^4 - T_{surr}^4\right)$ |
| $Q_{channel}$ | ±1.57 % | $\sigma\hat{F}(S + 2H)L\left(T_{surf}^4 - T_{amb}^4\right)$ |
| $\hat{F}$ | ±1.5 % | Given in equation 3.27 |
| $\overline{Nu}$ | ±8.17 % | $\frac{S\Delta Q}{A_{hs}\left(T_{surf} - T_{amb}\right)k_f}$ |
| $El$ | ±7.16 % | $\frac{g\beta\left(T_{surf} - T_{\mathrm{amb}}\right)S^3}{\nu\alpha}\frac{S}{L}$ |
| $\Delta Q$ | ±1 % | $P - Q_{rad}$ |
| $A_{hs}$ | ±0.1 % | $2B(W + L) + N(tL + 2tH + 2HL) + (N - 2)SL$ |

Table 5.3: Uncertainty of experimentally measured data

| Parameter | Range | Units | Maximum uncertainty | Comment |
|---|---|---|---|---|
| $V_{h_x}$ | 20 to 110 | V | ±0.03 % | Uncertainty in the FLUKE 8842a |
| $V_{R_x}$ | 0.035 to 1.100 | V | ±0.04 % | Uncertainty in the PCI-6229 device |
| $R$ | 1 | Ω | ±0.10 % | Manufacturer's quoted uncertainty |
| $T$ | 285 to 360 | K | ±0.1 K | Calibrated to this uncertainty using a 1504 thermistor. |
| $L$ | 0.3000 | m | ±0.5 mm | Uncertainty in the machining process of the Optimum BF46 Vario |
| $S$ | 0.0115 | m | ±0.5 mm | Uncertainty in the machining process of the Optimum BF46 Vario |
| $B$ | 0.0200 | m | ±0.5 mm | Uncertainty in the machining process of the Optimum BF46 Vario |
| $W$ | 0.1495 | m | ±0.5 mm | Uncertainty in the machining process of the Optimum BF46 Vario |
| $H$ | 0.0600 | m | ±0.5 mm | Uncertainty in the machining process of the Optimum BF46 Vario |
| $\varepsilon$ | 0.95 to 0.97 | | ±0.02 | Experimental values obtained in section 5.3 |

## 5.7. Summary

A list of all experimentally obtained values is given in table 5.2, and a list of experimentally derived values, using the method from Kline and McClintock in equation 5.7, and their formulae are given in table 5.3. The maximum uncertainty for the derived quantities of power dissipated, radiation, Nusselt number and Elenbaas number were 0.07 %, 7.1 %, 8.2 % and 7.2 % respectively and are displayed on the results presented in chapter 6.

# 6. Results and Discussion

This chapter is split into two sections; the first section, 6.1, discusses the results of a numerical parametric study on the thermal performance of a single heat sink equipped with a solar shield. The second section discusses the findings from an experimental and numerical investigation into an unshielded, shielded and secondary segregated structure, utilizing the findings from the parametric study.

## 6.1. Solar Shielding

In this section, results are presented and discussed in terms of heat dissipation from isothermal heat sink at 80 ℃ to ambient temperature of 55 ℃ as shown in figure 2.2 and discussed in section 2.1.1. The initial subsections explore the influence of time of day for the heat sink for a hot Summer's day in Kuwait, with and without a solar shield. Three subsections then present the effect of the geometric parameters which define the shield: length, vertical position of the heat sink within the shield, and clearance between the shield and the heat sink surfaces. The data for these investigations was obtained for the environmental conditions in Kuwait at the worst case time of day.

### 6.1.1. Time of Day

Figure 6.1 illustrates heat dissipation from the heat sink, with and without the solar shield, subject to the environmental conditions on the 15$^{th}$ of July 2011 in Kuwait, from noon to sunset. Peak solar irradiation occurred at noon (905 Wm$^{-2}$) and the peak ambient temperature (51 ℃) was at 13:30. At 13:30 the heat dissipation from the total heat sink reached its minima – 67.6 W and 67.8 W for the shielded and unshielded configurations, respectively. Note that the lower the total heat dissipation the worse the thermal performance. At this time, the solar irradiation and ambient temperature were 891.3 Wm$^{-2}$ and 51 ℃ respectively. The use of a shield increased the convective heat dissipation by an average of 4.9%, while also reducing solar loading from 15.76 W to 3.2 W at 15:30. The benefits were offset, however, by an increase in the shield temperature due to the solar loading which reduced the radiative heat dissipation by an average of 33.7%. The total heat dissipation from the unshielded heat sink surpassed the shielded heat sink when the solar irradiation (after 17:30) or the solar surface area (before 13:00) applied to the heat sink and shield was low. The orientation of the heat sink and shield configuration to south determines the solar ingress as a function of the time of day, and it is evident that orientation should be considered in any thermal

analysis based on representative environmental data, in order to form the basis of improved design practice.

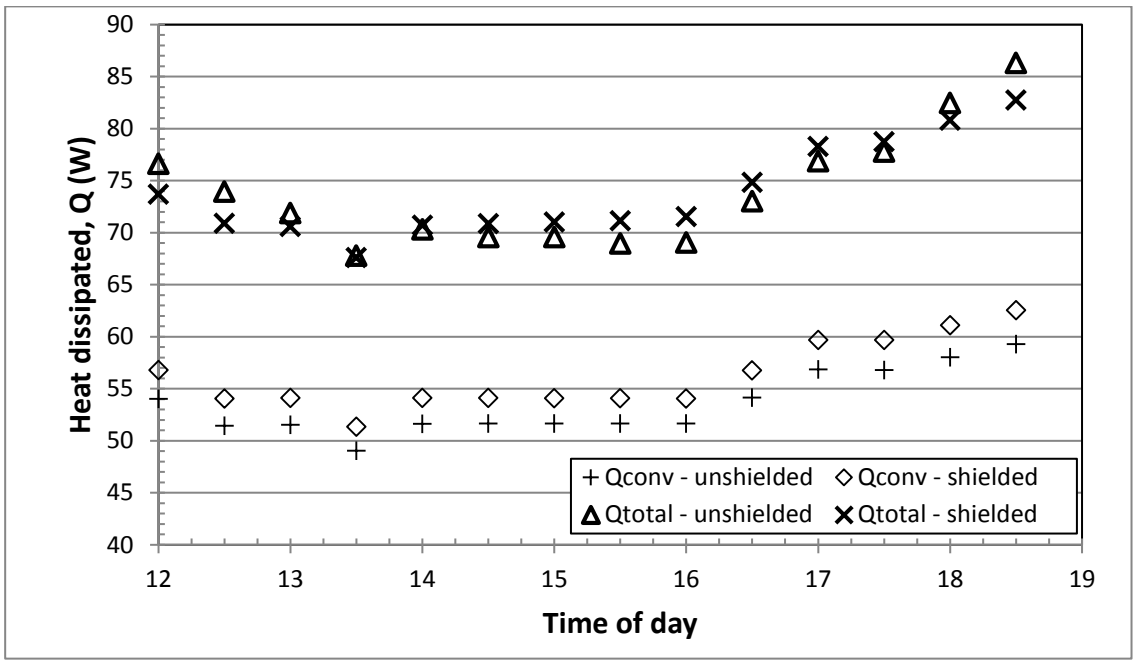


**Figure 6.1: Heat dissipation from the heat sink over the period noon to sunset in Kuwait on the 15th of July 2011**

Heat dissipation levels evaluated using the conditions of Telcordia GR-487 were far lower than those calculated for the representative environmental data at 13:30, the worst case time of day – values of 57.1 W and 56.9 W for the shielded and unshielded configurations, respectively.

It is evident that the use of these standard conditions is conservative in comparison with predictions based on the environmental data, a finding also found in Hawley & Palaszewski (2011). For the example under consideration here, the difference is 19.2 % – a discrepancy that would inspire the adaptation of a more comprehensive design process which references representative worst case environmental conditions.

### 6.1.2. Influence of Shielding

Figure 6.1 illustrates that the heat dissipation from the heat sink and shield configuration to ambient is higher than the unshielded case during the period from 14.00 to 17.30, with the maximum difference occurring at 16:00 – at which time the dissipation was 71.5 W and 69.1 W for the shielded and unshielded configurations, respectively. Although the shield reduces solar ingress during this period, it also serves to impair radiation from the surfaces of the heat sink to the surroundings, a mode which contributes strongly to the overall heat transfer, given the low convective heat transfer

rates associated with passive conditions. In the example under consideration in this thesis, the benefits of deploying a solar shield are relatively small – a 3.6 % difference in heat dissipation from the heat sink under worst case conditions – which may not prove compelling if cost is a constraint.

This finding correlates to the results of Naylor and Tarasuk (1993) and Lee and Yan (1994), who found that an isothermal plate in a chimney without adiabatic extensions offered a negligible improvement over an isothermal plate without a chimney.

### 6.1.3. Shield Length

The heat dissipation from the heat sink is plotted as a function of the length of the shield in figure 6.2, from a minimum of 300 mm (the same as the heat sink), to a maximum of 900 mm. In all cases, the vertical location of the heat sink was at the midpoint of the shield. The total heat dissipation in figure 6.2 increased with an increase in shield length due to a greater increase in the convective heat dissipation despite a reduction in the radiative heat dissipation. A 20.2 % increase in heat dissipation from the heat sink occurred, from 67.6 W to 81.3 W for the shield lengths of 300 mm and 900 mm respectively. Moreover, the dissipation was 13.5 W greater than that predicted for the unshielded case – an increase of 19.9 %. At a shield length of 700mm and 900mm, the shield absorbed all the solar irradiation while the radiative heat dissipation changed by <0.1%. The influence of the 'chimney flow' effect is evident as the total heat dissipation increased by 3% despite no practical changes in radiative heat dissipation or solar loading on the heat sink. In terms of practical applications, the deployment of a solar shield which is longer than the device that it contains would appear to be a feasible means of increasing heat dissipation – subject, of course, to practical considerations such as cost and wind loading.

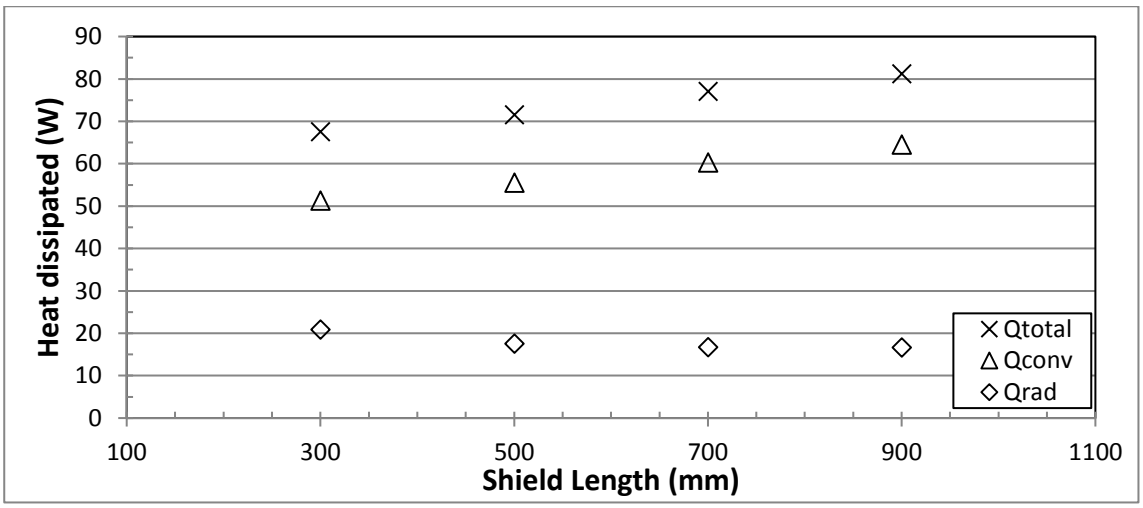


Figure 6.2: Heat dissipation from the sink as a function of shield length

### 6.1.4. Vertical Location of the Heat Sink

Figure 6.3 displays the heat dissipation from the heat sink as a function of the vertical position of the heat sink within the shield, for a fixed shield length of 900 mm. The position of the heat sink is moved vertically upwards from the base of the shield in steps of 100 mm to 600 mm, when the tops of the heat sink and the shield are in line. Dissipation from the heat sink decreases monotonically as the heat sink is positioned higher within the shield. In practice, if an extended shield is deployed, the device should be located close to the base of the shield, in order to maximise the benefits of chimney flow, as seen in Straatman *et al.* (1993). For the example under consideration in this thesis, an increase in heat dissipation of 38.6 % was found when compared to the unshielded case at 13:30 in the day.

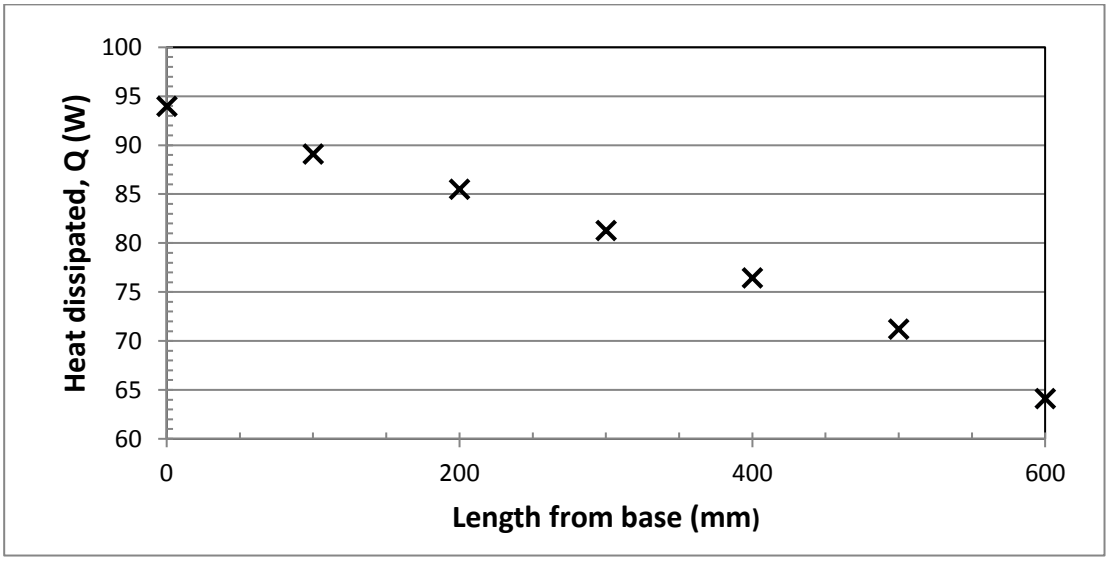


Figure 6.3: Heat dissipation from the sink as a function of vertical position of the sink within the shield, for a shield of length 900mm

### 6.1.5. Clearance

Heat dissipation from the heat sink is plotted as a function of the clearance between the surfaces of the shield and the heat sink in figure 6.4. For this investigation, the lengths of the heat sink and shield are at their default values, 300 mm. Some local minima and maxima are evident in the data – presumably the influence of boundary layer effects. It should be noted that the data spans a relatively small range (66.0 W to 70.3 W) indicating that clearance is of secondary importance as a design parameter in comparison with shield length and vertical location of the heat sink. Nevertheless, a maximum of 70.3 W dissipation was achieved for a clearance of 2 mm, an increase of 3.9 % over the value of 67.6 W attained at the default clearance of 5 mm.

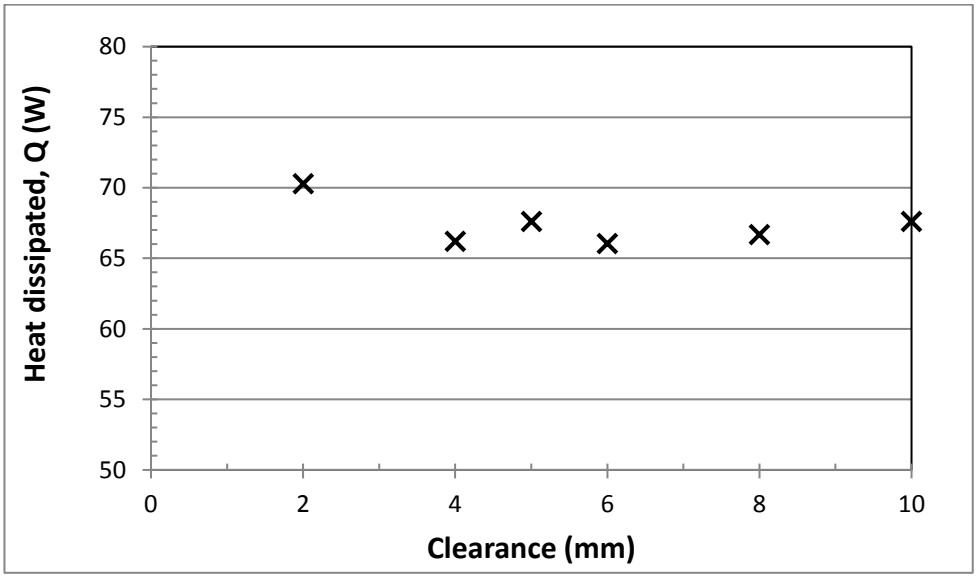


Figure 6.4: Heat dissipation from the sink as a function of clearance between the sink and the shield

## 6.2. Segregated Structure

In this section, results are presented and discussed in terms of heat dissipation from the primary heat sink to ambient, average Nusselt number of the primary heat sink, given in equation 3.7, and Nusselt ratio, given in equation 3.17. A constant temperature boundary condition is applied to the baseplate of the heat sink. The initial subsection confirms the validity of the experimentation and numerical techniques used, while the next subsection investigates the use of a shield to augment convective heat dissipation from a heat sink. The last subsection, section 6.2.3, then presents the effects of base plate temperature, location and the number of fins of the secondary heat sink on the primary heat sink.

### 6.2.1. Unshielded

Figure 6.5 plots the numerical, experimental and theoretical values for convective and radiative heat dissipation against the rise of the base plate temperature above ambient of an unshielded heat sink. The experimental values are within 7 % of the theoretical (Bar-Cohen & Rohsenow, 1984) and numerical values. The uncertainty in obtaining experimental total heat dissipation was less than 1 %, while the uncertainty for obtaining the theoretical values was 7 % due to uncertainties in the air properties calculated using the method outlined in section 5.6.3.

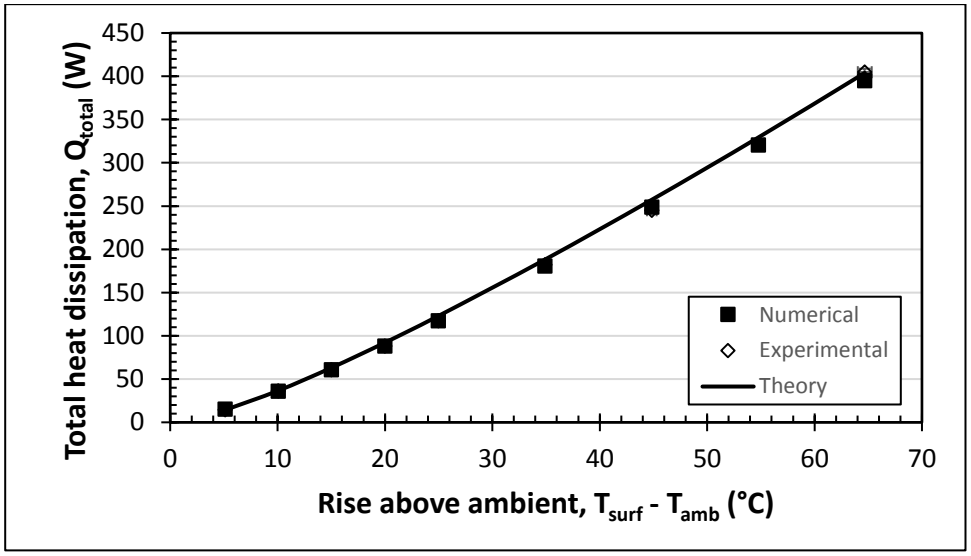


Figure 6.5: Total heat dissipated as a function of rise above ambient for a single unshielded heat sink

Correlated, numerical and experimental values for the Nusselt number of the primary heat sink are plotted as a function of the Elenbaas number in figure 6.6. Error bars represent the uncertainty in the experimental values, which exhibited maxima of 9 % and 7 % respectively in the Nusselt and Elenbaas numbers. The experimental and numerical values are within 10 % and 6 % of the correlation values respectively, an indication of the adequacy of the investigative methods used in this thesis. Two asymptotic limiting conditions exist, as noted in equation 3.11 in section 3.1, one where each fin acts as an isolated isothermal vertical flat plate and the other when the thermal boundary layers of each fin merge. At low Elenbaas, each fin acts like an isolated isothermal vertical flat plate which would alter the characteristic length from S to L, as noted by Elenbaas (Elenbaas, 1942), which results in a $Nu_s$ of less than 1.

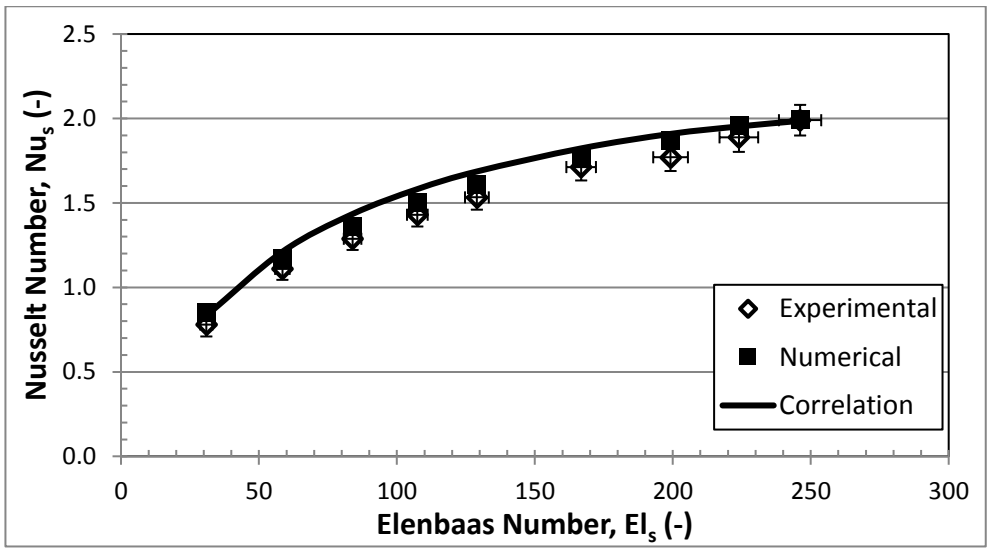


Figure 6.6: Nusselt number as a function of Elenbaas number for a single unshielded heat sink

### 6.2.2. Shielded

Figure 6.7 presents the Nusselt number as a function of Elenbaas number for a shielded and an unshielded heat sink. The unshielded values are the numerical values presented in figure 6.6. The experimental and numerical values for a shielded heat sink agree within 8 % of one another. The use of a shield augments the convective heat transfer by an average of 64 % in comparison with an unshielded sink. At lower Elenbaas numbers, the shielded structure offers the most improvement, greater than 70 %, however as the Elenbaas number increases, the enhancement diminishes to below 58 %. This agrees with the findings by Fischer and Torrance (1999) who suggested that a maximum performance increase exists for a specific chimney geometry, plate-to-plate spacing and Elenbaas number.

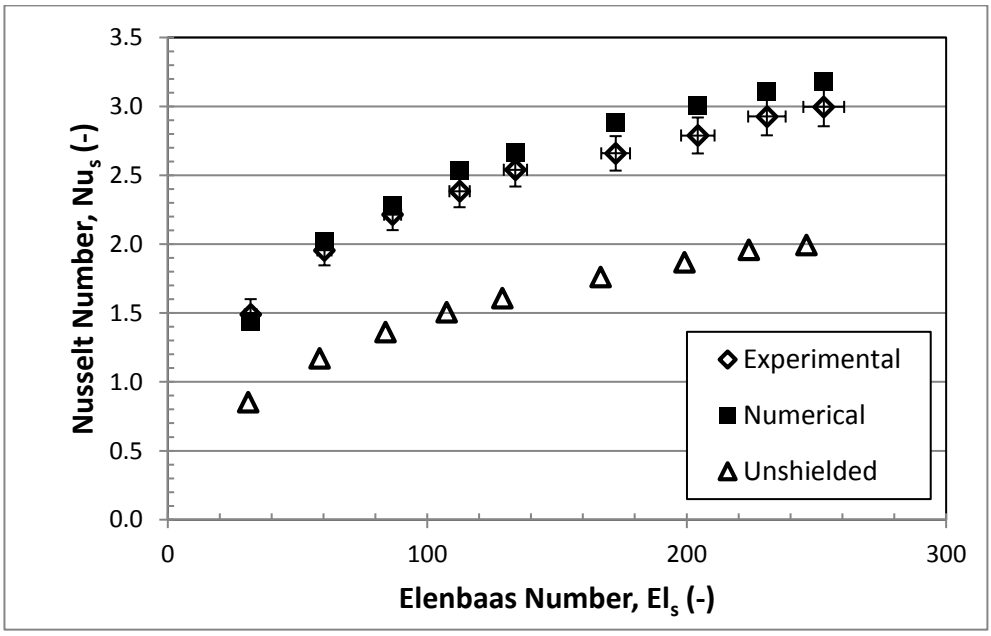

Figure 6.7: Nusselt number as a function of Elenbaas number for a shielded heat sink

### 6.2.3. Secondary Segregated Structure

The section presents the experimental and numerical results for a secondary segregated structure as shown in figure 5.3 in section 5.1.2. The first subsection discusses the Nusselt number of a primary heat sink with the addition of an unheated secondary heat sink. Subsection b) discusses the Nusselt number ratio of the primary heat sink with the addition of a set temperature on the base plate of a secondary heat sink. Subsection c) provides the Nusselt ratio of the primary heat sink at various secondary heat sink base temperature and gap distances. Finally, the last subsection, d), presents the numerical values for the Nusselt ratio as a result of the number of fins at the optimum location, found in the previous subsection, for a secondary heat sink with a base plate temperature of 65 ℃ above ambient.

#### *a) Unheated*

Figure 6.8 presents the numerical (squares) and experimental (diamond) Nusselt-Elenbaas data for a segregated structure with an unheated secondary heat sink. For comparison, numerical results for an unshielded (triangles) and a shielded (crosses) heat sink, replicated from figure 6.7, are also presented. A reduction of greater than 30 % in Nusselt number in comparison with a shielded case is evident; however the addition of an unheated secondary heat sink in a shielded structure still outperforms an unshielded sink. The additional flow resistance offered by the secondary sink within the shield evidently diminishes the Nusselt number of the primary heat sink. However, in this case, the maximum performance increase (38.5 %) over an unshielded heat sink occurs at an Elenbaas number of 200. This correlates to Naylor and Tarasuk (1993) who found that an increased Elenbaas number would diminish the effect of blockage. This blockage could be reduced by investigating different geometric properties for the secondary heat sink and the shield, such as a decreased secondary heat sink length and a non-uniform chimney like the one considered by Straatman *et al.* (1993).

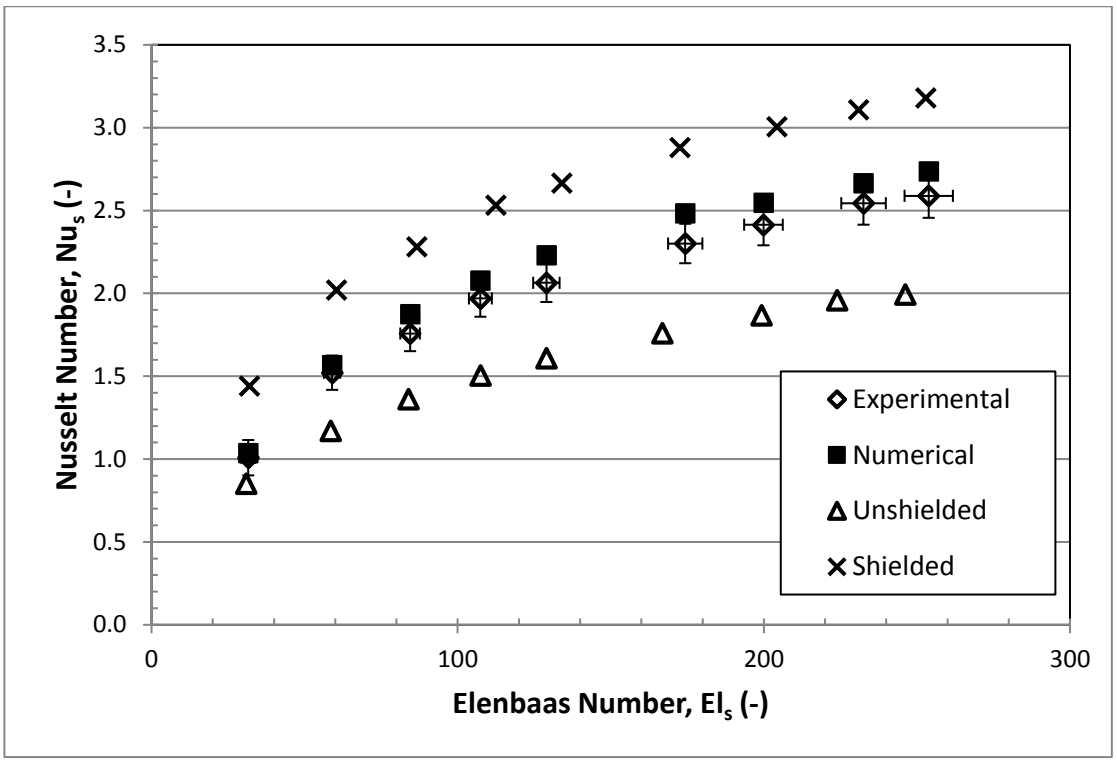


**Figure 6.8: Nusselt number as a function of Elenbaas number for a secondary segregated structure with an unheated secondary heat sink**

### *b) Heated*

In figure 6.9, the Nusselt ratio – a comparison of the numerical simulation against the baseline numerical case of the unshielded heat sink – for a 25 °C rise above ambient in the primary heat sink, the limit imposed by Telcordia-GR487, is plotted as a function of the base plate temperature of the secondary heat sink for four cases: unshielded, shielded, unheated secondary, and heated secondary.

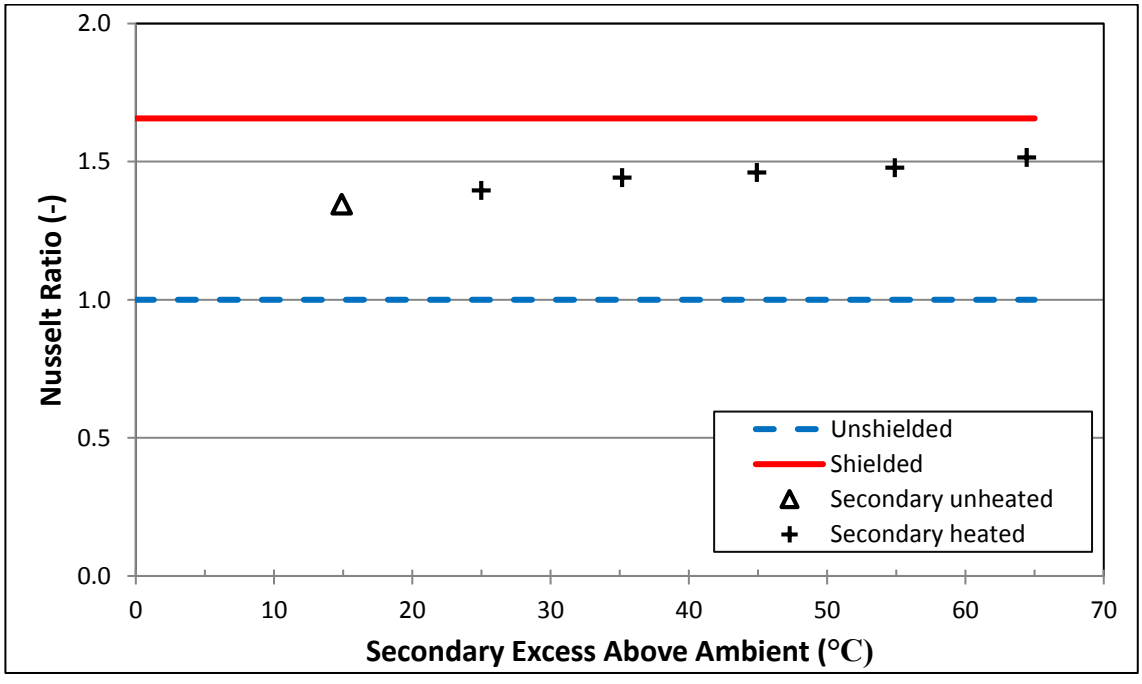

Figure 6.9: Experimental Nusselt ratio for a primary heat sink as a function of the secondary heat sink temperature

The Nusselt ratio exhibits an apparently linear increase in proportion to the temperature of the secondary heat sink, due to the additional mass flow induced by the secondary sink. At a secondary sink temperature of 65 °C above ambient, the limit of the variable under consideration in this thesis, an enhancement in the Nusselt number of ~50 % was observed in comparison with the baseline unshielded sink. This finding has practical utility: there is an evident advantage in segregating heat sinks within a representative outdoor wireless device to carry temperature sensitive and power devices on primary and secondary heat sinks, respectively, within a shielded structure that promotes chimney flow. As the base plate temperature of the secondary heat sink temperature rises, the Nusselt ratio increases, causing an enhancement to the convective heat transfer performance of the primary heat sink. This appeared as a linear trend indicating that further increases, in base plate temperature of the secondary heat sink to 115 degrees above ambient, would cause the Nusselt ratio of the primary heat sink to surpass the Nusselt ratio of the shielded heat sink. The rise above ambient required by the secondary heat sink to surpass the unsegregated structure would be reduced if the blockage, discussed in section a), could also be reduced. Triangular finned and pin fin heat sinks were found by Iyengar and Bar-Cohen (1998) to be superior to plate fins, an option which could reduce the blockage created by the heat sinks used in this thesis.

### c) Gap Distance

Figure 6.10 presents the numerical values of Nusselt ratio plotted against gap distance for an unshielded (blue dashed line), shielded (red line), unheated secondary heat sink (triangle) and a secondary heat sink with a base plate temperature of 65 ℃ above ambient (crosses). Studies by Naylor and Tarasuk (1993) indicate that heated components in a chimney structure should be located towards the inlet for the best performance. For a segregated structure, as suggested by the results, this appears to be the case. The idealised case of the secondary heat sink touching, but not conducting heat to, the primary heat sink provides an increase of over 75 % in the overall Nusselt ratio compared to an unshielded heat sink. A gap distance of 0mm is impractical as there would be conduction between the colder primary heat sink and the warmer secondary heat sink; the next highest Nusselt Ratio was seen at 50 mm.

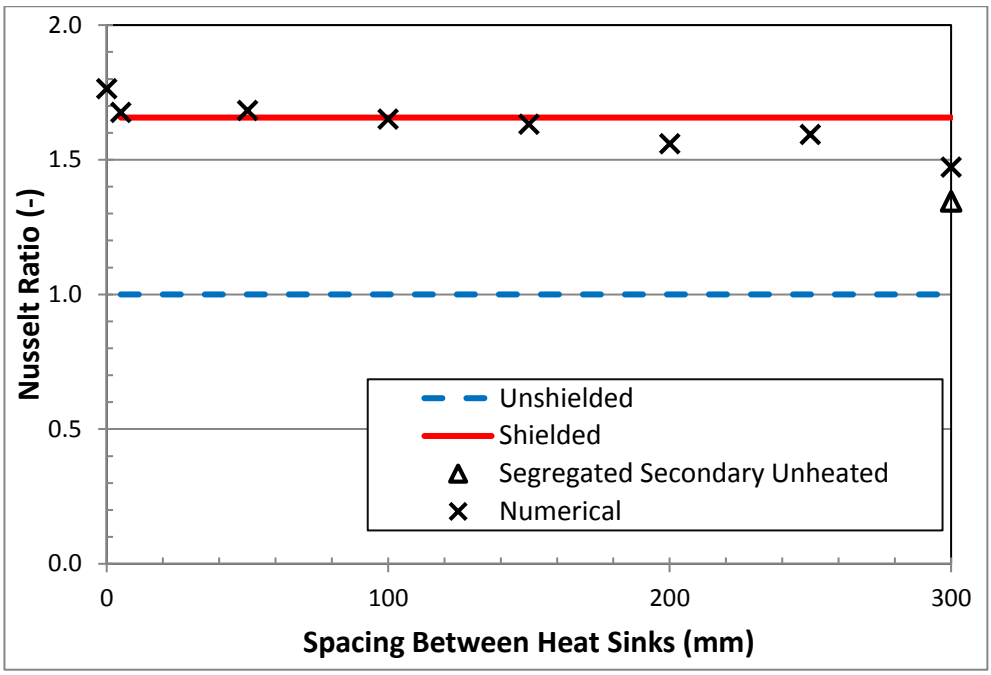


Figure 6.10: Nusselt ratio as a function of the spacing between the primary at 25°C above ambient and secondary heat sink at 65°C above ambient

### *d) Number of Fins*

Nusselt ratio, evaluated numerically, is presented in Figure 6.11 as a function of the number of fins on each side of the secondary heat sink at a gap distance of 50 mm. Numerical data for an unshielded sink and a shielded sink are also shown, with 12 on each side (24 in total). The optimum fin count for the secondary heat sink was found to be 8, or 16.7 mm spacing, which would appear to be a counterintuitive finding as the form of equation 3.15 would suggest that the higher the temperature of a sink, the smaller the optimum spacing. A secondary heat sink optimised for a 65 °C rise above ambient would require a spacing of under 9.6 mm, however this would neglect the temperature rise of the air caused by the primary heat sink. Thus, the secondary heat sink has a different local ambient temperature to the primary heat sink. At maximum local ambient temperature of the secondary heat sink, the primary heat sink base plate temperature, the secondary heat sink only experiences a 40 °C change in temperature and would need a spacing of 10.4 mm. However, the analysis presented here considers the behaviour of the primary and secondary heat sink in a segregated ensemble which has been optimised for a single isolated unshielded heat sink operating at 25 °C above ambient. Fischer and Torrance (1999) suggested, for a single shielded heat sink, that a maximum performance increase exists for a specific chimney geometry, plate-to-plate spacing and Elenbaas number; these results indicate that this holds true for a segregated

structure. The decrease in fins in the secondary heat sink, reduces the blockage created by the secondary heat sink, offering a performance increase as indicated by the addition of an unheated secondary heat sink in section 6.2.3a). The reduction of fin count also reduces the radiation from the secondary heat sink to the primary heat sink. As the heat sinks need to be designed to optimise flow, and as a consequence heat transfer, the optimum spacing of an unshielded heat sink is not the same as a primary heat sink in a segregated structure. The fin spacing on both the primary and secondary heat sinks would need to be investigated to ensure the flow is optimised. Additionally, different geometric properties of the heat sinks and shields could be investigated, in particular, keeping the segregated ensemble at the original 300 mm length as volume and weight are practical considerations for RRHs. Moreover, the heat sinks do not need to have the same length, in particular the secondary heat sink representing power amplifiers which are not highly temperature sensitive. Furthermore, a segregated structure does not need to have both heat sources at the same size or shape, nor does the shield need to have uniform width (slanted or curved walls for instance). There exists the potential to optimise the fin spacing and geometric properties of the primary heat sink in a segregated structure and, subsequently, the secondary heat sink, to further enhance heat transfer.

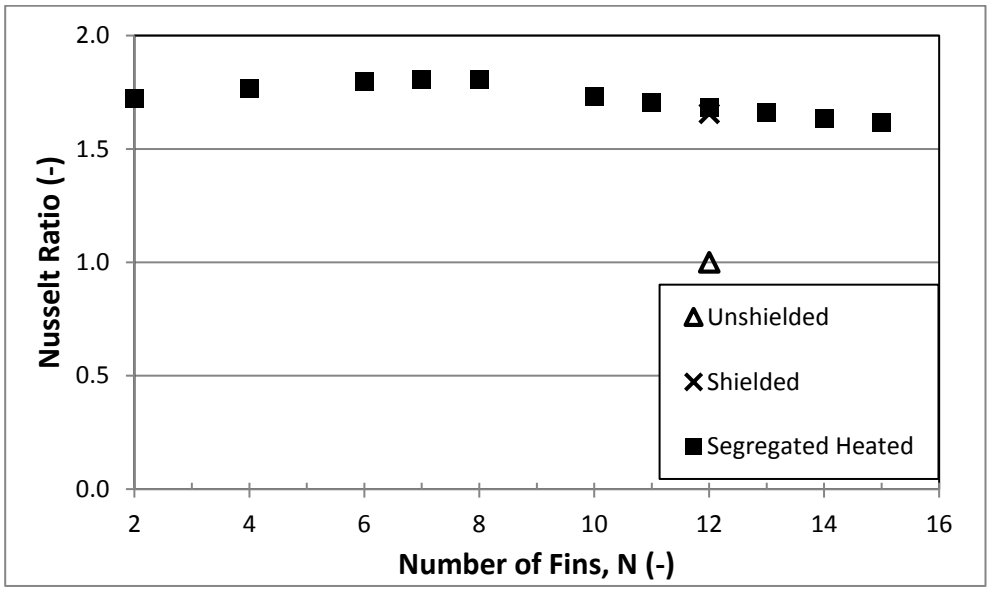


**Figure 6.11: Nusselt ratio as a function of the number of fins on each side of the secondary double sided heat sink**

## 6.3. Closure

The objective of the investigation was to explore the natural convection heat transfer from a heat sink representative of an RRH for a range of different environmental, geometrical and operational conditions. Numerical and experimental models were used to evaluate a heat sink in unshielded, shielded and segregated structures. It was found that a segregated structure with an increased plate-to-plate spacing in the secondary heat sink offered the greatest improvement in the Nusselt number of a primary heat sink. The results presented offer a contribution to an improved understanding of natural convection heat transfer in a segregated structure.

# 7. Conclusions and Recommendations

This chapter is split into two section, the first, section 7.1, provides the conclusions from this thesis while section 7.2 lists recommendations for future work.

## 7.1. Conclusions

In this thesis, a heat sink, representative of an RRH, was analysed for a range of different environmental, geometrical and operational conditions. The RRH was first analysed in a harsh environment with and without a solar shield, subject to different geometric and environmental conditions for a specific urban location at the hottest time of the year (Kuwait in summer). The geometric parameters investigated were shield length, vertical position and clearance; the environmental parameters were solar irradiation and orientation, and ambient temperature. The environmental standards of Telcordia GR-487 are considered relatively harsh, in particular when a solar shield was used. The RRH was then experimentally and numerically analysed in an unshielded heat sink configuration, a shielded configuration and in a secondary segregated structure. The parameters that were changed in the segregated structure were the secondary heat sink base plate temperature, gap distance and the number of fins on the secondary heat sink.

The conclusions for a RRH in a harsh environment are presented in subsection 7.1.1 while the conclusions of the RRH in a segregated structure are presented in subsection 7.1.2.

### 7.1.1. Solar Shield

- For a constant temperature boundary condition of 80 ℃ (25 ℃ over ambient) on the baseplate of the heat sink, the dissipation from the sink was found to be a strong function of time of day, reaching a minimum at 13:30. At this time, the solar irradiation and ambient temperature were below their daily maxima, yet the high projected area of the sink exposed to the sun resulted in high solar ingress. It is evident that orientation should be considered in any thermal analysis of outdoor wireless applications based on representative environmental data.
- Heat dissipation levels evaluated using the Telcordia GR-487 guidelines were lower by 19.2 % than those calculated for the representative environmental data at the worst case time of day. The adaptation of a more comprehensive design process which references representative worst case environmental conditions would appear to be worthwhile.

- Heat dissipation from the sink and shield configuration to ambient was higher than the unshielded case during the period from 14:00 to 17:30 (inferior performance), with a maximum difference of 3.59 % at 16:00. However, under worst case conditions at 13:30, the heat dissipation from the shielded configuration was 3.6% lower than the unshielded case (superior performance).
- The deployment of a solar shield which is longer than the device that it contains was found to increase heat dissipation through a 'chimney flow' effect and that the heat sink should be located at the base of the solar shield. For the example given, a 38.6 % increase in heat dissipation occurred when the length of the shield was extended to three times the sink length and the heat sink located at the base of the shield.

### 7.1.2. Segregated Structure

For the analysis of the segregated structure, heat sink geometries representative of a RRH were examined in terms of the enhancement in the Nusselt-Elenbaas behaviour of the primary sink. The following improvements were found when compared to the Nusselt number of an unshielded heat sink:

- The heat sink, when placed at the inlet of a shield three times the length of the heat sink, augmented the Nusselt number by an average of 64 % compared to the unshielded case. As the Elenbaas number increased, the augmentation decreased from greater than 70 % to less than 58 %.
- A secondary segregated structure with an unheated secondary heat sink reduced the Nusselt number of the primary heat sink by over 30 % compared to a shielded heat sink. Increasing the temperature of the secondary heat sink to 65 °C above ambient, increased the Nusselt number of the primary heat sink by over 50 % in comparison to an unshielded case.
- The location of the secondary heat sink in a segregated structure further enhanced the Nusselt number of a primary heat sink by over 75 % compared to an unshielded case. The optimum location was found to occur when no gap distance existed, however, this assumed no conduction between the two heat sinks. A small gap distance would be practical offering slightly better performance than a shielded heat sink.
- The number of fins on the secondary heat sink, in a segregated structure at the optimum gap distance and at a base plate temperature of over 65 ℃, offered an enhancement of 80 % over an unshielded heat sink. The maximum enhancement

occurred at 16 fins, resulting in a spacing of 19.2 mm. This highlights the potential to optimise the fin spacing of the secondary heat sink to further enhance heat transfer.

In conclusion, the outcome of this work is an improved understanding of a novel thermal management solution which is of practical relevance for the design of passively cooled outdoor wireless communication equipment.

## 7.2. Recommendations

As discussed in section 6.2.3, the heat sinks need to be designed to optimise flow and, as a consequence, heat transfer. The optimum number of fins on the secondary heat sink was investigated in this thesis, however, this merely served to maximise the output of the primary heat sink under investigation. The fin spacings for both the primary and secondary heat sinks would influence flow and the heat transfer. The optimum spacing of an unshielded heat sink is not the same as the primary heat sink in a segregated structure. As the primary heat sink carries temperature sensitive components in practice, an accurate number of fins spacing on the primary heat sink is of utmost importance.

Practically, operators on a base tower are charged for volume, weight and size of the RRH unit. This investigation did not consider the volume, weight or size limitations that typical RRH designers would face. Moreover the heat sinks do not need to have the same length, in particular the secondary heat sink representing power amplifiers which are not highly temperature sensitive. Reduction of the size of the segregated structure down to 300 mm in length and optimising the secondary and primary heat sinks number of fins, lengths and gap distance would be of practical importance.

Furthermore, a segregated structure does not need to have both heat sources at the same size or shape, nor does the shield need to be uniform in section. There exists the potential to utilise different heat sinks combinations (pin fin, plate, staggered, radial) or shield configurations (slanted, curved) to achieve an optimum practical configuration.

# 8. References


Agonafer, K. P., Lakhkar, N., Agonafer, D. & Morrison, A., 2010. Solar shroud design using computational fluid dynamics. *12th IEEE Intersociety Conference on Thermal and Thermomechanical Phenomena in Electronic Systems (ITherm)*, 2010 Las Vegas.

Amer, E. H., 2006. Passive options for solar cooling of buildings in arid areas. Energy, Volume 31, pp. 1332-1344.

Asaina, T. et al., 2010. Development of WiMAX Remote Radio Heads. *SEI TECHNICAL REVIEW 71*.

Asako, Y., Nakamura, H. & Faghri, M., 1990. Natural convection in a vertical heated tube attached to a thermally insulated chimney of a different diameter. *Journal of Heat Transfer*, 112(3).

ASHRAE, 2009. ASHRAE Handbook - Fundamentals (SI).

Bacharoudis, E. et al., 2007. Study of the natural convection phenomena inside a wall solar chimney with one wall adiabatic and one wall under a heat flux. *Applied Thermal Engineering*, Issue 27, pp. 2266-2275.

Bar-Cohen, A. & Rohsenow, W. M., 1981. Thermally optimum spacing of vertical, natural convection cooled, parallel plates. *Heat transfer in electronic equipment; Proceedings of the Winter Annual Meeting*, Washington, pp. 154-158.

Bar-Cohen, A. & Rohsenow, W. M., 1984. Thermally optimum spacing of vertical, natural convection cooled, parallel plates. *Journal of Heat Transfer*, Issue 106, pp. 116-123.

Bejan, A., 2004. *Convection Heat Transfer*. 3rd ed. Wiley, John & Sons.

Brackenridge, M., 2011. *SunPosition Calculator.* [Online] Available at: http://www.sunposition.info/sunposition/spc/locations.php [Accessed 11 November 2011].

Brydson, J. A., 2000. *Plastics Materials.* 7th ed. Oxford: Butterworth-Heinemann.

Cd-Adapco, 2010. *STAR-CCM+ User Guide Version 6.02.007.* [Online] Available at: https://steve.cd-adapco.com [Accessed 05 March 2012].

Cisco Systems, 2013. *Cisco Visual Networking Index: Global Mobile Data Traffic Forecast Update, 2012–2017*.

Commscope, 2012. *Active Antennas: The Next Step in Radio and Antenna Evolution*.

Elenbaas, W., 1942. Heat dissipation of parallel plates by free convection. *Physica*, 9(1).

Ellison, G., 1979. Generalized computations of the gray body shape factor for thermal radiation from a rectangular U-channel. *IEEE Transactions on Components, Hybrids, and Manufacturing Technology*. 2(4) pp. 517–522.

Ericsson, 2016. *Mobile Traffic*. [Online] Available at: https://www.ericsson.com/mobility-report/mobile-traffic [Accessed 24 May 2012].

Fischer Elektronic, 2016. *SK 92/150 SA Heat Sink.* [Online] Available at: http://www.fischerelektronik.de/en/home-en/ [Accessed 2016].

Fisher, T. S. & Torrance, K. E., 1999. Experiments on chimney-enhanced free convection. *Journal of Heat Transfer*, 121(3).

Fisher, T. S., Torrance, K. E. & Sikka, K. K., 1997. Analysis and optimization of a natural draft heat sink system. *IEEE Transactions on Components, Packaging, and Manufacturing Technology Part A*, 2(20).

Ghosh, A. et al., 2012. Heterogeneous cellular networks: From theory to practice. *IEEE Communications Magazine*, 50(6), pp. 54-64.

Guglielmini, G., Nannei, E. & Tanda, G., 1987. Natural convection and radiation heat transfer from staggered vertical fins. *International Journal of Heat and Mass Transfer*, pp. 1941-1948.

Haaland, S. E. & Sparrow, E. M., 1983. Solutions for the channel plume and the parallel-walled chimney. *Numerical Heat Transfer*, 6(2).

Hawley, F. & Palaszewski, S., 2011. Characterization of realistic environmental conditions for predicting the reliability of outdoor cellular electronics. *Electronics Cooling*, pp. 12-17.

Hubbard, K. G., Lin, X. & Walter-Shea, E. A., 2001. The effectiveness of the ASOS, MMTS, Gill, and CRS air temperature radiation shields. *Journal of Atmospheric and Oceanic Technology*, Volume 18, pp. 851-864.

Incropera, F. P., DeWitt, D. P., Bergman, T. L. & Lavine, A. S., 2011. *Fundamentals of Heat and Mass Transfer*. 7th ed. John Wiley & Sons.

Iyengar, M. & Bar-Cohen, A., 1998. Least-material optimization of vertical pin-fin, plate-fin, and triangular-fin heat sinks in natural convective heat transfer. *The Sixth Intersociety Conference on Thermal and Thermomechanical Phenomena in Electronic Systems, ITHERM 1998*. Seattle.

Khor, Y. K., Hung, Y. M. & Lim, B. K., 2010. On the role of radiation view factor in thermal performance of straight-fin heat sinks. *International Communications in Heat and Mass Tranfer*, Volume 37, pp. 1087-1095.

Kim, T. H., Kim, D.-K. & Do, K. H., 2013. Correlation for the fin Nusselt number of natural convective heat sinks with vertically oriented plate-fins. *Heat and Mass Transfer*, 49(3), pp. 413-425.

Kline, S. J. & McClintock, F. A., 1953. Describing uncertainties in single-sample experiments. *Mechanical Engineering*, 1(75).

Kumar, A., 2014. *Mobile Broadcasting with WiMAX: Principles, Technology, and Applications*. 1st ed. CRC Press.

La Pica, A., Rodono, G. & Volpes, R., 1993. An experimental investigation on natural convection of air in a vertical channel. *International journal of heat and mass transfer*, 36(3), pp. 611-616.

Ledezma, G. & Bejan, A., 1997. Optimal geometric arrangement of staggered vertical plates in natural convection. *Journal of Heat Transfer*, Volume 119, pp. 700-708.

Lee, K. T., 1994. Natural convection in vertical parallel plates with an unheated Entry or unheated exit. *Numerical Heat Transfer*, 25(4), pp. 477-493.

Lee, K. T. & Yan, W. M., 1994. Laminar natural convection between partially heated vertical parallel plates. *Wärme-und Stofföbertragung*, 29(3), pp. 145–151.

Malhammer, A., 1987. Optimum sized air channels for natural convection cooling. *The Ninth International Telecommunications Energy Conference, INTELEC 1987*. Stockholm.

Mariam, F., Raju, U., Mulay, V. & Agonafer, D., 2009. Thermal design considerations of air-cooled high powered telecommunications cabinets. *25th Annual IEEE SEMI-THERM 2009*, pp. 222-227.

Marongiu, M. J., Kusha, B., Helm, R. & Waiter, K., 1998. Design and development of a passively cooled remote outdoor cabinet. *Twentieth International Telecommunications Energy Conference (INTELEC).*

Marsters, C. F., 1975. Natural convective heat transfer from a horizontal cylinder in the presence of nearby walls. *The Canadian Journal of Chemical Engineering*, 53(1) pp. 144–149.

Moore, F. K., 1973. Minimum size of large dry cooling towers with combined mechanical and natural draft. *Journal of Heat Transfer*, 95(3), pp. 383-389.

Nasrallaha, H. A., Nieplovab, E. & Ramadanc, E., 2004. Warm season extreme temperature events in Kuwait. *Journal of Arid Environments*, Volume 56, pp. 357-371.

Naylor, D. & Tarasuk, J. D., 1993a. Natural convective heat transfer in a divided vertical channel. I: Numerical study. *Journal of Heat Transfer*. 115(2), pp. 377-387.

Naylor, D. & Tarasuk, J. D., 1993b. Natural convective heat transfer in a divided vertical channel. II: Experimental study. *Journal of Heat Transfer*. 115(2), pp. 388-394.

Oosthuizen, P. H., 1984. A numerical study of laminar free convective flow through a vertical open partially heated plane duct. *ASME HTD*, 32(4).

Ostrach, S., 1953. An analysis of laminar free-convection flow and heat transfer about a flat plate parallel to the direction of the generating body force. *naca-report-1111*.

Praught, R. B., 1982. Inclined fins for a more efficient heat sink. *International Telecommunications Energy Conference (INTELEC) 1982*. Washington D.C. pp. 158-164

Rajkumar, M. R., Venugopal, G. & S., A. L., 2013. Natural convection from free standing tandem planar heat sources in a vertical channel. *Applied Thermal Engineering*, 50(1) pp. 1386-1395.

Rea, S. N. & West, S. E., 1976. Thermal radiation from finned heat sinks. *IEEE Transactions on Parts, Hybrids and Packaging*, 12(2), pp.115-117.

Shabany, Y., 2008. Radiation heat transfer from plate-fin heat sinks. *Twenty-fourth Annual IEEE Semiconductor Thermal Measurement and Management Symposium*. San Jose, pp. 133-137.

Shabany, Y., 2010. *Heat Transfer; Thermal Management of Electronics*. Boca Raton Florida: Taylor & Francis Group.

Sparrow, E. M. & Bahrami, P. A., 1980. Experiments on natural convection from vertical parallel plates with either open or closed edges. *Journal of Heat Transfer*, 102(2), pp. 221-227.

Sparrow, E. M. & Prakash, C., 1980. Enhancement of natural convection heat transfer by a staggered array of discrete vertical plates. *Journal of Heat Transfer*, 102(2), pp. 215-220.

Straatman, A. G., Tarasuk, J. D. & Floryan, J. M., 1993. Heat transfer enhancement from a vertical, isothermal channel generated by the chimney effect. *Journal of Heat Transfer*, 115(2), pp. 395-402.

Sumitomo Electric, 2012. [Online] *Sumitomo Electric Develops Remote Radio Head for TD-LTE Base Stations* Available at: http://global-sei.com/news/press/12/prs013_s.html [Accessed 9 November 2015].

Telcordia Technologies, 2009. *Generic Requirements for Electronic Equipment Cabinets*. GR-487-CORE, Issue 3.

Texas Instruments, 2011. *Block Diagram - Telecom Tower: Remote Radio Unit (RRU).* [Online] Available at: http://www.ti.com/solution/telecom_tower_remote_radio_unit_rru [Accessed 9 November 2015].

Thrasher, W. W., Fisher, T. S. & Torrance, K. E., 2000. Experiments on chimney-enhanced free convection from pin-fin heat sinks. *Journal of Electronic Packaging*, 122(4), pp.350-355.

Vermeersch, B., De Mey, G., Wójcik, M., Pilarski, J., Lasota, M., Banaszczyk, J., Napieralski, A. and De Paepe, M., 2008. Chimney effect on natural convection cooling of electronic components. *IMAPS Advanced Technology Workshop on Thermal Management,* pp. 1-6).

Weather Underground, Inc., 2011. *History: Weather Underground*. [Online] Available at: http://www.wunderground.com/history/airport/OKBK/2011/7/15/DailyHistory [Accessed 11 November 2011].

Zapach, T., 2009. Thermal and Mechanical Design Considerations *TEKTELIC Communications Inc.*

# Appendix A: Published Papers

- O'Flaherty, K. and Punch, J. (2014) "The Use of Segregated Heat Sink Structures to Achieve Enhanced Passive Cooling for Outdoor Wireless Devices", Journal of Physics: Conference Series, 525(1), 012019: doi:10.1088/1742-6596/525/1/012019.
- O'Flaherty, K. and Punch, J., 2012, "The Influence of Solar Shielding on the Thermal Behavior of Outdoor Communications Equipment", Proceedings of ITherm 2012: Thirteenth Intersociety Conference on Thermal and Thermomechanical Phenomena in Electronic Systems, San Diego, CA, USA, May-June, doi: 10.1109/ITHERM.2012.6231553.

# Appendix B: Calibration Certificate for Multimeters

**Calibration Specialists Limited**
**Out of Tolerance Notification**

**Make:** FLUKE

**Model:** 8842A

**S/N:** 4545025

**Ref. No.** N/A

**Cert No.** 1311065

**Customer:** UNIVERSITY OF LIMERICK

**Instrument Description:** MULTIMETER

**Out of Tolerance:**

**Upon receipt it was not possible to take any DC current measurements. At all other points this unit meets specification.**

Calibration Eng: David Mullins Date: 22/11/13

Date sent to Engineering:

Engineering Sign Off: Date:

Procedure: OTN-CSL Control No. 4833 Rev. No. 2.00 – Date: 18/01/2013

# Appendix C: Calibration Certificate for FLUKE 1504

Fluke Corporation
799 E Utah Valley Drive
American Fork, Utah 84003-9775

**Fluke Calibration, American Fork**
**Primary Temperature Lab**
**Report of Calibration**

NVLAP®
For the Scope of Accreditation
Under NVLAP Lab Code 200348-0

| Model: | Serial No.: | Customer: |
|---|---|---|
| 1504 | B29859 | FLUKE NEDERLAND B.V.<br>SON 5692<br>NL |
| Description: Readout, Digital Thermometer | | |
| Received Condition: New | Procedure: HCT106 - 0 | As Left Condition: In Tolerance |

The above referenced digital thermometer readout or readout module was calibrated by one of two methods. Resistance instruments were calibrated by direct measurement of laboratory resistance transfer standards and/or comparison to a high precision ratio bridge. Thermocouple instruments were calibrated by precision voltage excitation and reference junction compensation measurements. The calibration data and internal calibration coefficients are shown on the following page(s) of this report. Any limitations or remarks pertaining to this instrument or calibration are shown below. The test uncertainty ratio (TUR) of this calibration is at least 4:1 unless otherwise indicated. This calibration is traceable to NIST, ratiometric techniques, or natural physical constants and is in compliance to ISO/IEC 17025:2005 and ANSI/NCSL Z540-1. This calibration certificate applies only to the item described and shall not be reproduced other than in full, without written approval of Fluke Calibration, American Fork. This calibration certificate shall not be used to claim product endorsement by NVLAP or any agency of the U.S. Government. Calibration certificates without signatures are not valid.

*Test Equipment*

| Instrument | Model | Serial No. | Recall Date |
|---|---|---|---|
| Thermistor Probe | 5610 | A511290 | 11/29/2012 |
| Standard Resistor Set | 3591 | A1C003 | 11/09/2012 |
| Precision Digital Thermometer | 1529-R | A27259 | 01/08/2013 |
| Test Station | N/A | 2 | NCR |

Environmental Conditions:
Temperature: 23°C
Humidity: 44% RH
Calibration Date: 09/19/2012
Calibration Due: Not Defined
PO #: 610143585-FCO-0/GB//S J E
Report No: B2924045

Performed by: Levi Dillman

Approved by: Roger Sims
Calibration Technician

Page: 1 of 2

*This report shall not be reproduced except in full without written approval of Fluke Calibration, American Fork.*

# Appendix D: Air properties

The air properties taken throughout this thesis are interpolated from the table D.1 below (Bejan, 2004).

Table D.1: Air properties from 0 to 120°C (Bejan, 2004)

| Celsius (°C) | Density (kg/m$^3$) | specific heat (kJ/kg.K) | thermal conductivity (W/m.K) | kinematic viscosity (m$^2$/s) | thermal expansion coefficient (1/K) |
|---|---|---|---|---|---|
| 0 | 1.293 | 1005 | 0.0243 | 1.33E-05 | 0.00367 |
| 20 | 1.205 | 1005 | 0.0257 | 1.51E-05 | 0.00343 |
| 40 | 1.127 | 1005 | 0.0271 | 1.70E-05 | 0.00320 |
| 60 | 1.067 | 1009 | 0.0285 | 1.89E-05 | 0.00300 |
| 80 | 1.000 | 1009 | 0.0299 | 2.09E-05 | 0.00283 |
| 100 | 0.946 | 1009 | 0.0314 | 2.31E-05 | 0.00268 |
| 120 | 0.898 | 1013 | 0.0328 | 2.52E-05 | 0.00255 |